



UNIVERSITY OF LEEDS

This is a repository copy of *Kinetics of the Reaction of OH with Isoprene over a Wide Range of Temperature and Pressure Including Direct Observation of Equilibrium with the OH Adducts*.

White Rose Research Online URL for this paper:
<http://eprints.whiterose.ac.uk/135198/>

Version: Accepted Version

Article:

Medeiros, DJ, Blitz, MA orcid.org/0000-0001-6710-4021, James, L et al. (2 more authors) (2018) Kinetics of the Reaction of OH with Isoprene over a Wide Range of Temperature and Pressure Including Direct Observation of Equilibrium with the OH Adducts. *Journal of Physical Chemistry A*, 122 (37). pp. 7239-7255. ISSN 1089-5639

<https://doi.org/10.1021/acs.jpca.8b04829>

© 2018 American Chemical Society. This document is the Accepted Manuscript version of a Published Work that appeared in final form in *Journal of Physical Chemistry A*, copyright © American Chemical Society after peer review and technical editing by the publisher. To access the final edited and published work see <https://doi.org/10.1021/acs.jpca.8b04829>. Uploaded in accordance with the publisher's self-archiving policy.

Reuse

Items deposited in White Rose Research Online are protected by copyright, with all rights reserved unless indicated otherwise. They may be downloaded and/or printed for private study, or other acts as permitted by national copyright laws. The publisher or other rights holders may allow further reproduction and re-use of the full text version. This is indicated by the licence information on the White Rose Research Online record for the item.

Takedown

If you consider content in White Rose Research Online to be in breach of UK law, please notify us by emailing eprints@whiterose.ac.uk including the URL of the record and the reason for the withdrawal request.



eprints@whiterose.ac.uk
<https://eprints.whiterose.ac.uk/>

Kinetics of the Reaction of OH with Isoprene over a Wide Range of Temperature and Pressure Including Direct Observation of Equilibrium with the OH Adducts

D.J. Medeiros,¹ M.A. Blitz,^{*1,2} L. James,¹ T.H. Speak,¹ P.W. Seakins^{*1,2}

1 - School of Chemistry, University of Leeds, Leeds, LS2 9JT, UK.

2 – National Centre for Atmospheric Science, University of Leeds, Leeds, LS2 9JT, UK.

Abstract

The reaction of the OH radical with isoprene, C₅H₈ (R1), has been studied over the temperature range 298 - 794 K and bath gas pressures of nitrogen from 50 - 1670 Torr using laser flash photolysis (LFP) to generate OH, and laser induced fluorescence (LIF) to observe OH removal. Measurements have been made using both a conventional LFP/LIF apparatus and a new high pressure system. The measured rate coefficient at 298 K ($k_{1,298\text{ K}} = 9.90 \pm 0.09 \times 10^{-11} \text{ cm}^3 \text{ molecule}^{-1} \text{ s}^{-1}$) in the high pressure apparatus is in excellent agreement with the literature confirming the accuracy of measurements made with this instrument.

Above 700 K, the OH decays were no longer single exponentials due to regeneration of OH from adduct decomposition and the establishment of the OH + C₅H₈ \rightleftharpoons HOC₅H₈ equilibrium, R1a/R-1a. This equilibrium was analysed by comparison to a master equation model of reaction R1, and determined the well-depth for OH addition to carbon C₁ and C₄ to be equal to (153.5 \pm 6.2) kJ mol⁻¹ and (143.4 \pm 6.2) kJ mol⁻¹, respectively. These well-depths are in excellent agreement with the present ab initio - CCSD(T)/CBS//M062X/6-311++G(3df,2p) - calculations (154.1 kJ mol⁻¹ for the C₁ adduct). Addition to the less stable C₂ and C₃ adducts are not important.

The data above 700 K also indicated that a minor, but significant direct abstraction channel, R1b, was also operating with $k_{1b} = (1.3 \pm 0.3) \times 10^{-11} \exp\left(\frac{-3.61 \text{ kJ mol}^{-1}}{RT}\right) \text{ cm}^3 \text{ molecule}^{-1} \text{ s}^{-1}$. Additional support for the presence of this abstraction channel comes from our ab initio calculations and from room-temperature proton transfer mass spectrometry product analysis.

The literature data on reaction R1 together with the present data were assessed using master equation analysis, using the MESMER package. This analysis produced a refined dataset that generates our recommended $k_{1a}(T,[M])$. An analytical representation of $k_{1a}(T,[M])$ and $k_{-1a}(T,[M])$ is provided via a Troe expression. The reported experimental data (the sum of addition and abstraction), $k_1^\infty = (9.5 \pm 0.2) \times 10^{-11} \left(\frac{T}{298 \text{ K}}\right)^{-1.33 \pm 0.07} + (1.3 \pm 0.3) \times 10^{-11} \exp\left(\frac{-3.61 \text{ kJ mol}^{-1}}{RT}\right) \text{ cm}^3 \text{ molecule}^{-1} \text{ s}^{-1}$, significantly extends the measured temperature range of R1.

*Authors to whom correspondence should be addressed. m.a.blitz@leeds.ac.uk, p.w.seakins@leeds.ac.uk.

1 Introduction

The diene isoprene, C₅H₈, is the dominant biogenic hydrocarbon emission.¹⁻² Isoprene reacts rapidly with the OH radical (R1, $k_{298\text{ K}} = (1.00 \pm 0.15) \times 10^{-10} \text{ cm}^3 \text{ molecule}^{-1} \text{ s}^{-1}$)³ and, in the presence of NO_x, can lead to significant local air quality issues, particularly ozone formation.⁴



In low NO_x/high isoprene environments such as forests, where there is a rapid loss route for OH with isoprene, but no obvious route for OH regeneration, it was expected that ambient [OH] would be low. However, campaigns in a variety of such environments ranging from boreal forests⁵ to Mediterranean pine forests,⁶ to rain forests⁷⁻⁸ have measured surprisingly high concentrations of OH, with the measured:modelled [OH] being up to 10:1.⁷ These observations suggest a mechanism for OH regeneration; the implications of a higher concentration of ambient OH on methane lifetimes, and hence on radiative forcing, are significant.⁹

A range of mechanisms¹⁰ including OH production from RO₂ + HO₂ reactions¹¹, RO₂ photolysis¹² and epoxide formation from OH + isoprene adducts¹³ have been investigated. These processes provide some enhancement of OH levels, but do not bridge the gap between measurement and model. Currently the most promising mechanism for explaining OH regeneration is the Leuven Isoprene Mechanism (LIM), proposed by Peeters and co-workers.¹⁴⁻¹⁵ Under low NO_x conditions the OH-isoprene-O₂ radical formed in reactions R1a-R2, can isomerize to form a hydroperoxycarbonyl (HPALD) / dihydroperoxycarbonyl (di-HPCARP) species that lead to OH regeneration.



The reactions of HOC₅H₈O₂ take place on minute/hour timescales at room temperature and it is difficult, even with the most careful experiments, to eliminate the possibility of contributions from heterogeneous processes or secondary chemistry. Additionally, in some chambers it is not possible to avoid a contribution from NO_x driven chemistry,¹⁶ so the resulting product distribution can be complex and identifying the products from low NO_x chemistry can be difficult. However, given the importance of quantifying the HO_x budget in tropical regions, quantitative validation of the role of the LIM1¹⁵ mechanism is required.

An alternative approach to mechanism validation is to use direct techniques at higher temperatures to observe OH regeneration (via HOC₅H₈O₂ isomerization for isoprene oxidation) on millisecond timescales in flash photolysis experiments.¹⁷ Under these conditions there can be no contribution from heterogeneous processes and NO_x can be rigorously excluded. However, to drive the isomerization chemistry to the millisecond timescale, high temperatures must be used and this has a consequent effect in the high concentration of oxygen required to ensure a substantial concentration of HOC₅H₈O₂ as reaction R2 reaches equilibrium conditions. The resulting high pressures and concentrations of O₂ make conventional observation of OH by laser induced fluorescence (LIF) difficult, due to quenching of the fluorescence signal. However, we have recently developed a new high pressure flash photolysis reactor based on

the FAGE technique, where OH is sampled into a low pressure region before detection by LIF,¹⁸ such that measurements can be made under these conditions.

Reaction R1, at least at low temperatures (<600 K), occurs predominantly by a pressure dependent addition mechanism, with addition to the two terminal carbon (C₁ and C₄) being dominant due to the formation of stabilized allylic radicals. At high temperatures, abstraction from the methyl group (R1b), again forming an allylically stabilized radical, may contribute.



At high enough pressures, the rate limiting step is the association reaction to form the chemically activated adduct with a corresponding high pressure rate coefficient, k_{1a}^∞ . For a large system such as R1, with a strongly bound adduct, this high pressure limit is reached at low absolute pressures (e.g. <1 Torr at room temperature). At higher temperatures, the rate coefficient for dissociation of the chemically activated adduct increases significantly, becoming competitive with stabilization and the reaction can exhibit pressure dependence.

Previous work at ambient temperature on the kinetics of the OH + isoprene reaction is generally in excellent agreement. IUPAC recommends a room temperature rate coefficient of $(1.00 \pm 0.15) \times 10^{-10} \text{ cm}^3 \text{ molecule}^{-1} \text{ s}^{-1}$.³ Measurements have been made by both direct laser flash photolysis methods and relative rate techniques, with the later having used a range of different reference reactions. Reaction R1 appears to be at its high pressure limit above 50 – 100 Torr at room temperature, however, there is some controversy as to the onset of the pressure independent region.¹⁹⁻²² There is no evidence of any significant role for the abstraction reaction at room temperature.

The objectives of this work are to further characterise the high pressure apparatus by comparison with the well-studied room temperature OH + isoprene addition reaction and to generate data on reaction R1 at the higher temperatures required to observe OH recycling in the presence of O₂ on the millisecond timescale (450 - 630 K), where little or no experimental data are available. Furthermore, direct observation of OH regeneration from the OH adduct at high temperatures, allows for a determination of the well depth of the HOC₅H₈ adduct. The returned adduct well depth is compared with that from ab initio calculations. Both experiment and theory are used to investigate whether there is evidence for any contribution to R1 from abstraction, R1b. Finally, to use the master equation (ME) programme, MESMER, to compare previous measurements of reaction R1.²³

The paper is organized according to the following description. Section 2 describes the experimental (2.1) and computational (2.2) methods used. The experimental analysis and data are presented in two sections: Section 3.1 presents data where OH profiles are simple exponential decays, Section 3.2 reports on the OH traces obtained under equilibrium conditions. The results and discussion are sub-divided into several sections. The ab initio calculations are presented in Section 4.1 providing an overview of the reactions (addition and

abstraction) and the relative importance of the different addition channels. Section 4.2 compares our experimental data with the literature. Section 4.3 presents the experimental evidence for an abstraction channel, as the analysis of the equilibrium data (Section 4.4) requires an understanding of all the OH removal processes. Section 4.4 also reports the experimentally determined well-depth and discusses the model dependence of the results. Finally, in Section 4.5 we present the ME analysis of all the literature data and an analytical representation of k_1 as a function of temperature and pressure.

2 Experimental and Computational Methods

2.1 Experimental

A significant number of experiments were carried out in our recently developed high temperature, high pressure reactor and full details of the apparatus can be found in Stone et al.¹⁸ Briefly, the apparatus consisted of a heatable flow tube ($T = 298 - 700$ K, $p = 300 - 2000$ Torr) through which a mixture of OH precursor, H_2O_2 (50% (w/w) Sigma Aldrich), isoprene (Sigma Aldrich, >99%) and nitrogen bath gas were flowed. OH radicals were generated along the flow tube by pulsed excimer laser (Lambda Physik, Compex 200) photolysis at 248 nm, although a few experiments used a YAG laser (Quantel, Q-smart laser) at 266 nm to generate OH radicals from H_2O_2 photolysis. A fraction of the gas flow was sampled from the end of the flow tube through a 0.05 mm pinhole and into a low pressure (~ 1 Torr) observation chamber. Here the gas stream from the pinhole was interrogated 5 mm from the pinhole by a pulsed (5 Hz) beam from a YAG pumped dye laser system (Spectron, operating on the dye rhodamine 6G), tuned to ~ 282 nm to match a rovibrational channel in the A – X transition of OH. The resulting fluorescence at ~ 308 nm was passed through a filter (Barr Associates, (308 ± 5) nm) and collected on a channel photomultiplier tube (Perkin-Elmer C1943P), mounted perpendicularly to the gas stream and probe radiation beam. The delay between the photolysis and probe pulses was systematically varied by a delay generator (BNC 555) to build up an OH time profile (see inset to Fig. 2 for a typical example) including information on the pre-photolysis background level of OH. Each trace typically consisted of 270 points (with 20 points providing pre-trigger background) and the final trace was typically an average of 5 – 10 repetitions.

The OH radical precursor, predominantly H_2O_2 , was delivered from a temperature stabilized bubbler and the approximate concentration ($\sim 1 \times 10^{15}$ molecule cm^{-3}) determined from the removal of OH measured in the absence of isoprene. Based on the precursor concentration, laser energy density (~ 15 mJ cm^{-2} or $\sim 2 \times 10^{16}$ photons cm^{-2}), the precursor cross-section ($\sim 1 \times 10^{-19}$ cm^2 molecule $^{-1}$ for H_2O_2)²⁴ and quantum yield, (2 for OH production from H_2O_2), the initial OH concentration was estimated to be $\sim 4 \times 10^{12}$ molecule cm^{-3} , significantly below the isoprene concentration, ensuring pseudo-first order conditions. Isoprene mixtures were made up manometrically in 10 litre stainless steel high pressure cylinders and left to mix for 48 hours prior to use. The isoprene concentration in the reactor

was determined from the measured flowrates through calibrated mass flow controllers, the cylinder composition and the measured pressure in the reactor.

Experiments were also carried out at lower pressures ($p = 50 - 150$ Torr, $T = 300 - 794$ K) in a conventional laser flash photolysis apparatus where the OH was observed in situ by LIF. Details on the operation of this apparatus can be found in Onel et al.²⁵⁻²⁶ In this case, isoprene/N₂ mixtures were prepared in a darkened 5 litre bulb. As an instrumental check, tertiary-butyl hydroperoxide was also used as the OH precursor at 298 K to ensure the measured coefficients are independent of the implemented precursor. The enhanced sensitivity of this lower pressure apparatus meant that lower concentrations of H₂O₂ ($\sim 1 \times 10^{14}$ molecule cm⁻³) could be used. Experiments were carried out under conditions where OH was lost by a simple pseudo-first-order process and also at sufficiently high temperatures such that direct equilibration between OH/isoprene and the OH-C₅H₈ adducts was observed. Such experiments provide strong constraints on the thermochemistry of the reaction.²⁷

Additionally, proton-transfer reaction time of flight mass spectrometry (Kore Technology, Series I PTR-TOF-MS), was employed for a qualitative verification of the product of the allylic hydrogen abstraction by OH radicals. The exhaust gas from the high pressure high temperature apparatus, described previously¹⁸ was vented to atmospheric pressure and subsequently sampled into the PTR-MS spectrometer.

2.2 Computational Methods: Ab initio Calculations and Master Equation (ME) Modelling

Fully optimized structures of reactants and products were computed with the modern DFT functional M06-2X²⁸ and a large basis set (6-311++G(3df,2p)).²⁹ Structure optimizations were carried out using the Gaussian 09 D.01 programme suite³⁰, with the use of analytical gradients and the Berny algorithm³¹⁻³² in redundant internal coordinates. High performance coupled cluster calculations with single, double and triple excitations, the latter treated perturbatively (CCSD(T)),³³ were implemented to calculate single point energies of M06-2X/6-311++G(3df,2p) optimized geometries. For a more accurate evaluation of the potential energy surface (PES), the single point energies were extrapolated to the complete basis set limit (CBS) using the extrapolation scheme presented by Helgaker et al.³⁴ and Truhlar's calendar basis sets (Jun-cc-pVXZ, X=D,T,Q).³⁵⁻³⁶ These basis set variations are constructed by removing diffuse functions from the analogue fully augmented basis set (aug-cc-pVXZ). More specifically, the Jun-cc-pVXZ basis sets remove the diffuse functions from H and He atoms and also remove the highest angular momentum diffuse functions from all the other atoms. A slight deviation from the original formulation of the calendar basis sets is considered by Gaussian 09 since by default, s and p diffuse functions are always introduced. In the extrapolation scheme presented by Helgaker et al., the Hartree-Fock (HF) and the correlation energies are extrapolated separately, according to equations E1 and E2. The employed Hartree-Fock extrapolation scheme was originally presented by Feller et al.³⁷

$$\text{HF}(X) = \text{HF}_{\text{CBS}} + b \exp(-cX) \tag{E1}$$

$$E_{\text{CORR}}(X) = E_{\text{CORR(CBS)}} + \alpha X^{-3}$$

E2

where $\text{HF}(X)$ is the Hartree-Fock energy calculated with the jun-cc-pVXZ basis set. X is the cardinal number for the basis set (2=D, 3=T, 4=Q). The CBS limit extrapolated Hartree-Fock energy (HF_{CBS}), b and c are parameters obtained from solving the 3x3 system of HF equations.

$E_{\text{CORR}}(X)$ is the correlation energy calculated at the CCSD(T)/Jun-cc-pVXZ level of theory.

$E_{\text{CORR(CBS)}}$ corresponds to the CBS limit correlation energy and α is a floated parameter. Zero-point energies, force-constant matrices, vibrational frequencies and rotational constants, required inputs for the ME calculations were computed at the M06-2X/6-311++G(3df,2p) level as expensive CCSD(T) calculations would be computationally prohibitive.³⁸ However, the use of the M06-2X functional coupled with an extensive basis set has been considered appropriate for the study of the isoprene + OH reaction in the presence of O_2 ¹⁵, and the photolysis of important products of this reaction, such as HPALDs.³⁹ Harmonic vibrational frequencies were corrected with a scaling factor of 0.983, following the recommendation for a similar methodology (M06-2X/6-311++G(d,p)).⁴⁰

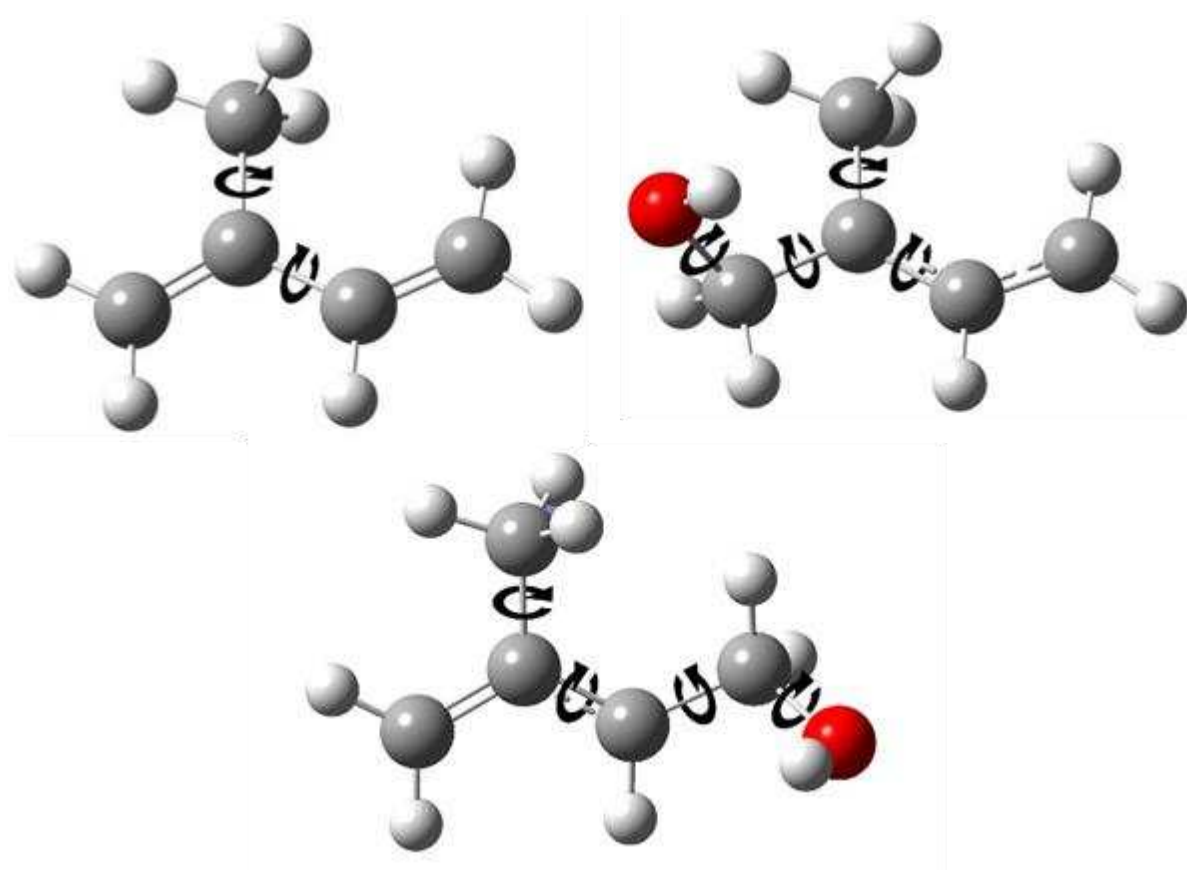


Figure 1. The rotational torsions described with the hindered rotor approximation (black curved arrows) for isoprene (top left), the isoprene-OH adduct 1 (top right) and the adduct rising from OH addition to carbon 4 (bottom). Grey, red and white spheres represent carbon, oxygen and hydrogen atoms respectively. The structure of the higher energy adducts formed following OH addition at carbons 2 and 3 are presented as Cartesian coordinates in the Supplementary Information.

The approximation of the harmonic oscillator was used for the majority of the vibrational frequencies in the calculation of the densities of states. However, due to the structures of the stabilized allylic radicals, a few vibrational frequencies of isoprene and the resulting adducts are better represented by the hindered rotor approximation. For example, the $>C_1=C_2<$ double bond in the isoprene structure has a single-bond analogue in the product structure, which provides an augmented torsional degree of freedom to the molecule, with respect to this bond. Figure 1 shows all the torsions that were described with the hindered rotor approximation for both isoprene and the two most stable isoprene-OH adducts considered in the analysis. The descriptions of these hindered rotors were obtained through 360° relaxed scans of the dihedral angle respective to the specific rotation, with steps of 15° . Restricted optimizations at the M06-2X/6-311++G(3df,2p) level were applied at each step. In order to avoid inconsistency in the number of degrees of freedom of species in the ME calculations, the description of a hindered rotor requires the removal of a corresponding vibrational frequency. MESMER uses the projection method proposed by Sharma et al.⁴¹ to define the mode related to the internal rotation.

Pressure dependent reactions can be modelled with the ME method.⁴²⁻⁴³ The energies of the reagents and C_5H_8 -OH adducts are divided into grains, a typical grain width being ~ 50 cm^{-1} ; a series of coupled differential equations then links the energy grains of the adduct. Each grain can be populated or de-populated by collisional energy transfer into another energy grain of the adduct, additionally each grain can also be populated by the pseudo-first-order chemical reaction of OH and isoprene and de-populated by re-dissociation to reagents. The probability of energy transfer between grains i,j is determined by the exponential down model (i.e. the probability decreases exponentially dependent on the energy separation between i and j) with reverse probabilities determined by detailed balance. The energy transfer parameter $\langle\Delta E\rangle_{d,M}$ is given by $\langle\Delta E\rangle_{d,M} = A_{\langle\Delta E\rangle_{d,M}} \times (T/298)^m$, being its temperature dependence, m , fixed to typical values according to the implemented bath gas (1.00, 0.30 and 0.25 for He, Ar and N_2 respectively).²³ The limited pressure dependence observed in the temperature range covered by this investigation would prevent a precise estimate of this parameter. $A_{\langle\Delta E\rangle_{d,M}}$ depends on the bath gas used, however, it is possible to assign different values to each bath gas and hence to compare experimental studies using different bath gases. The microcanonical, energy dependent, rate coefficients, $k(E)$, linking reagents and adducts are related to the thermal rate coefficients via an inverse Laplace transformation.

In general terms, the energy grained master equation (EGME) can be described as:

$$\frac{dp}{dt} = \mathbf{M}p \tag{E3}$$

where p is the population density vector and \mathbf{M} , the transition matrix, describes the evolution of the population over time due to reaction and collisional energy transfer. The solution of E3 yields:

$$p = Ue^{\Lambda t}U^{-1}p(0) \quad \text{E4}$$

where U is a matrix of eigenvectors obtained by the diagonalization of M , Λ is the vector of corresponding eigenvalues and $p(0)$ contains the initial conditions for each grain. MESMER solves the EGME and extracts the phenomenological rate coefficients from the chemically significant eigenvalues. The selection of these eigenvalues is made by the procedure described by Bartis and Widom.⁴⁴ Information on parameters used can be found in an example MESMER script in the Supplementary Information.

3 Data Analysis

3.1 Single Exponential Traces

At temperatures below 650 K, OH reacted under pseudo-first-order conditions via a simple removal process; in this regime, the concentration of OH as a function of time is given by:

$$[\text{OH}]_t = [\text{OH}]_0 e^{-k_1' t} \quad \text{E5}$$

where k_1' is the pseudo-first-order rate coefficient given by:

$$k_1' = k_1[\text{C}_5\text{H}_8] + k_{1\text{st}} \quad \text{E6}$$

Here k_1 is the bimolecular rate coefficient for reaction R1 and $k_{1\text{st}}$ represents the rate coefficient for the loss processes due to diffusion and reaction of OH with the constant concentration of precursor, k_p . As the OH LIF signal is proportional to $[\text{OH}]$, the $[\text{OH}]$ in E5 can be replaced by the OH LIF signal and the resulting exponential fit (inset to Figure 2) to the LIF data, returns k_1' . Under these conditions, a plot of k_1' vs $[\text{C}_5\text{H}_8]$ should give a straight line, as shown in Figure 2, where the gradient is k_1 and the intercept is the sum of the first order loss processes. The resulting k_1 rate coefficients are summarised in Table 1.

Table 1. Experimental Determinations of k_1 from Single Exponential Decays

T / K	p / Torr	$k_1 \times 10^{11} / \text{cm}^3$ molecule ⁻¹ s ⁻¹ a	T / K	p / Torr	$k_1 \times 10^{11} / \text{cm}^3$ molecule ⁻¹ s ⁻¹ a
298	1290	9.90 ± 0.14	473	99	4.98 ± 0.36
298	1365	10.01 ± 0.12	475	1394	5.61 ± 0.50
298	96 ^b	10.60 ± 0.36	477	128	5.3 ± 1.0
298	56	10.40 ± 0.32	478	114	6.12 ± 0.36
337	57	8.28 ± 0.22	508	1673	5.7 ± 1.2
406	1367	6.68 ± 0.54	533	132	4.91 ± 0.24
417	1497	7.2 ± 1.6	540	141	5.27 ± 0.36
418	1418	6.24 ± 0.34	564	1350	4.74 ± 0.44
426	103	5.56 ± 0.26	573	51	4.4 ± 1.1
433	1546	6.0 ± 1.5	618	1536	3.99 ± 0.46
472	99	5.81 ± 0.86	630	1373	4.71 ± 0.56

a – Errors are 2 σ . b – Data where p < 150 Torr were recorded on the low pressure, conventional LFP/LIF apparatus. Other data were from the high pressure apparatus.

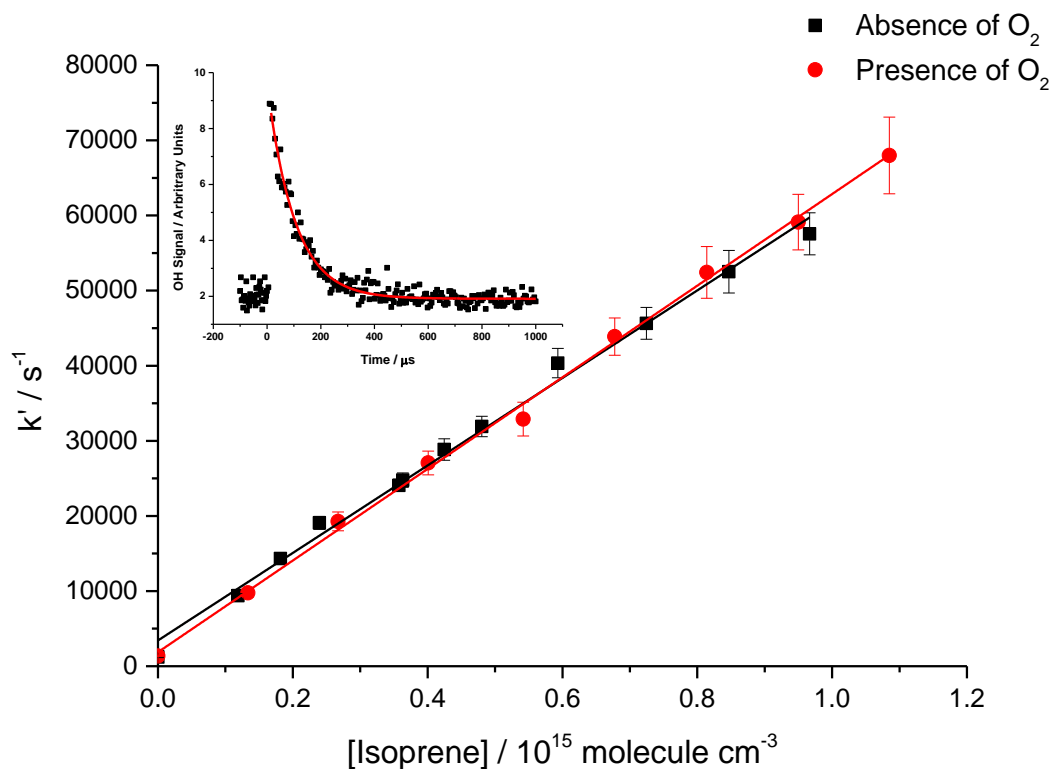
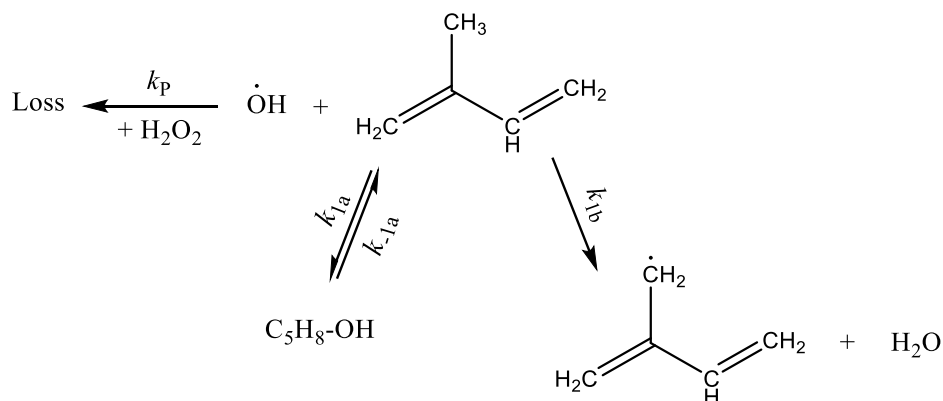


Figure 2. Bimolecular plot for reaction R1 at $T = 406$ K and $p = 2$ atm of N_2 . The inset shows a typical single exponential decay, generated with $[C_5H_8] = 1.00 \times 10^{14}$ molecule cm^{-3} and $[O_2] = 7.70 \times 10^{18}$ molecule cm^{-3} . The points presented in the inset were averaged after 4 scans. Error bars in the bimolecular plot are at the 2σ level. Red circles represent data acquired in the presence of oxygen and black squares represent data in absence of O_2 .

3.2 High temperature equilibrium traces

At high enough temperatures ($T > 700$ K), the rates of decomposition of the OH- C_5H_8 adducts (R-1a) become comparable with that of the forward addition of OH to isoprene and the OH decays become multi-exponential in nature (see Figure 3 for an example). The obtained equilibrium traces were analysed by fitting to the chemical scheme S1:



S1

where C₅H₈-OH represents the OH-isoprene adduct. As will be reported in Section 4.4, additions to the C₂ and C₃ carbons are negligible and can be ignored. A kinetic scheme incorporating two adducts would be a triexponential decay, but if the properties of the adducts are similar, then the decays can be well approximated by a biexponential decay. As expected, the experimental data were not better fitted with a tri-exponential equation, so our data were analysed based on models derived from Scheme S1; the role of both adducts 1 and 4 is assessed via MESMER modelling in Section 4.4.

The analytical solution of the temporal evolution of the OH concentration in scheme S1 is described by the bi-exponential equation E7:

$$\text{OH}(t) = \text{OH}_0 \left(\frac{-k'_{\text{OH}} - \lambda_-}{\lambda_+ - \lambda_-} (\exp(\lambda_+ t) - \exp(\lambda_- t)) + \exp(\lambda_- t) \right) + b \quad \text{E7}$$

where $\lambda_{-,+} = \frac{-(k'_{\text{OH}} + k_3) \pm \sqrt{(k'_{\text{OH}} + k_3)^2 - 4(k'_{\text{OH}} k_3 - k'_{1a} \times k_{-1a})}}{2}$, $k'_{\text{OH}} = k'_{1a} + k'_D$, and $k_3 = k_{-1a}$. k'_{1a} is the pseudo-first order rate coefficient for the addition channel of reaction R1, k'_D is the sum of the pseudo-first order OH losses besides addition, $k_D = k_{1st} + k_{1b}'$, where k_{1st} is the sum of the OH reaction with the precursor ($k_p[\text{H}_2\text{O}_2]$) and diffusion, (which is small compared to $k_p[\text{H}_2\text{O}_2]$), and k'_{1b} is the rate coefficient of the hydrogen abstraction channel of reaction R1 and is equal to $k_{1b}[\text{C}_5\text{H}_8]$. b is equal to the signal when no OH is present. For each temperature and pressure, k_{1st} was measured prior to the OH-trace acquisition with added isoprene; k_{1st} was fixed to its measured value in the data fitting procedure. b was determined for each trace by recording points before time zero (the photolysis pulse).

Over the temperature range 729 – 794 K, a total of 28 traces were recorded that exhibited equilibrium behaviour. Figure 3 clearly demonstrates non-single exponential behaviour at 729 K and 130 Torr of N₂. The red line is a fit using equation E7 to the data, and as can be seen, it provides an excellent description of OH temporal behaviour. From equation E7, λ_+ is the numerically larger reciprocal time constant and is approximately equal to k'_1 and the smaller reciprocal time constant, λ_- , is approximately equal to $k_D + k'_{1b}$. In Figure 3, the green line is the significantly poorer fit when the abstraction channel, k'_{1b} , is set to zero. It is evident that abstraction is required in order to describe the chemistry of the system; this abstraction channel is discussed in Sections 4.3 and 4.4. Therefore, the parameters k_{1a} , k_{-1a} and k_{1b} along with the initial OH signal are required to provide a good fit to the data.

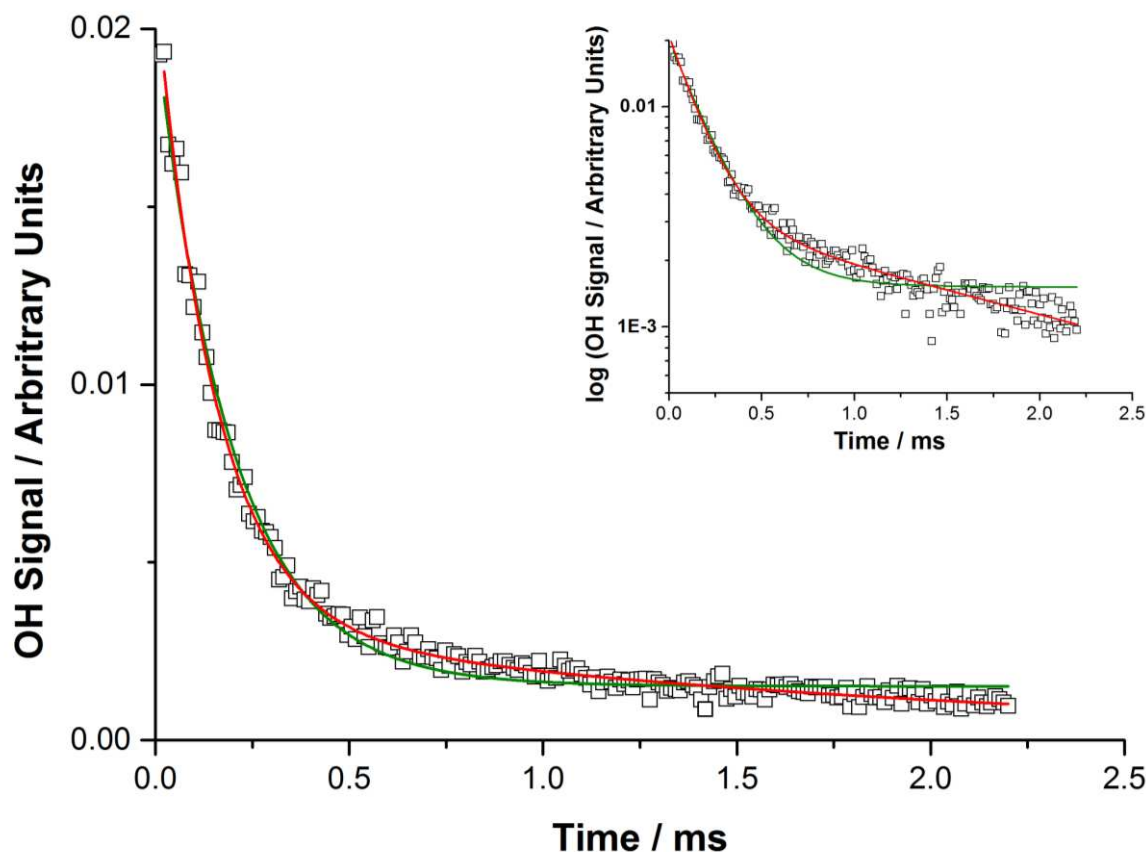


Figure 3. Example of a non-exponential trace acquired at $T = 729$ K, $p = 130$ Torr N_2 and $[\text{isoprene}] = 2.3 \times 10^{14}$ molecule cm^{-3} . The inset shows the same decay trace with a logarithmic scale for the OH signal. The long-time decay of OH shows that there is a significant process by which OH is lost from the system (modelled as k_{1b}). The green lines shows fits of equation E7 to the data where the abstraction was suppressed and the red lines represent fits where the abstraction was considered.

In order to reliably determine the parameters, all the equilibrium traces were simultaneously analysed via a global non-linear multi-temperature least-squares fit procedure, using the OriginPro 2016 software.⁴⁵ For the global fitting, the addition rate coefficient as a function of temperature was assigned the flexible function:

$$k_{1a}(T) = A_{1a} (T/298)^n \quad \text{E8}$$

where k_{1a} was fixed to the room temperature value, 1.0×10^{-10} cm^3 molecule $^{-1}$ s $^{-1}$. Both the adduct dissociation and the abstraction rate coefficients can be parameterized by Arrhenius expressions:

$$k_{-1a}(T) = A_{-1a} \times \exp(-E_{-1a}/RT) \quad \text{E9}$$

$$k_{1b}(T) = A_{1b} \times \exp(-E_{1b}/RT) \quad \text{E10}$$

However, the temperature range is too small for both Arrhenius parameters to be uniquely defined. Therefore, A_{-1a} was fixed to 10^{13} s $^{-1}$ and E_{1b} was fixed to 3.6 kJ mol $^{-1}$, the theoretical value calculated in this study, see Section 4.1. Other fixed Arrhenius values could have been

chosen but they would all generate, within error, the same values for $k_{-1a}(T)$ and $k_{1b}(T)$ over the experimental temperature range. Therefore, only three rate coefficient parameters, plus the initial OH signal were adjusted in this global analysis. The results are summarized in Table 2. Examples of global analysis fits to the data are shown in Figure 4. The Arrhenius parameterization allows global fits over a range of temperatures, but primarily generates values of $k_{-1a}(T)$ to input into the MESMER analysis (section 4.4). It is these rate coefficients, not the Arrhenius parameters, which are used to define the well depth in Section 4.4.

Table 2. Experimental conditions, number of $\text{OH} + \text{C}_5\text{H}_8 \rightleftharpoons \text{HOC}_5\text{H}_8$ equilibrium traces and obtained rate coefficients.

T / K	p / Torr	[isoprene] / 10^{14} molecule cm^{-3}	OH Loss / s^{-1}	Number of traces	$k_{1a} \times 10^{11} / \text{cm}^3 \text{ molecule}^{-1} \text{ s}^{-1}$	k_{-1a} / s^{-1}	$k_{1b} \times 10^{12} / \text{cm}^3 \text{ molecule}^{-1} \text{ s}^{-1}$
729	100	1.3-5.0	100	6	1.77 ± 0.74	990 ± 870	6.94 ± 2.77
729	130	1.6-6.0	220	6	1.77 ± 0.74	990 ± 870	6.94 ± 2.77
766	120	0.5-3.9	80	9	1.61 ± 0.68	3000 ± 2600	7.14 ± 2.78
794	100	1.2-5.0	110	7	1.50 ± 0.63	6500 ± 5500	7.29 ± 2.79

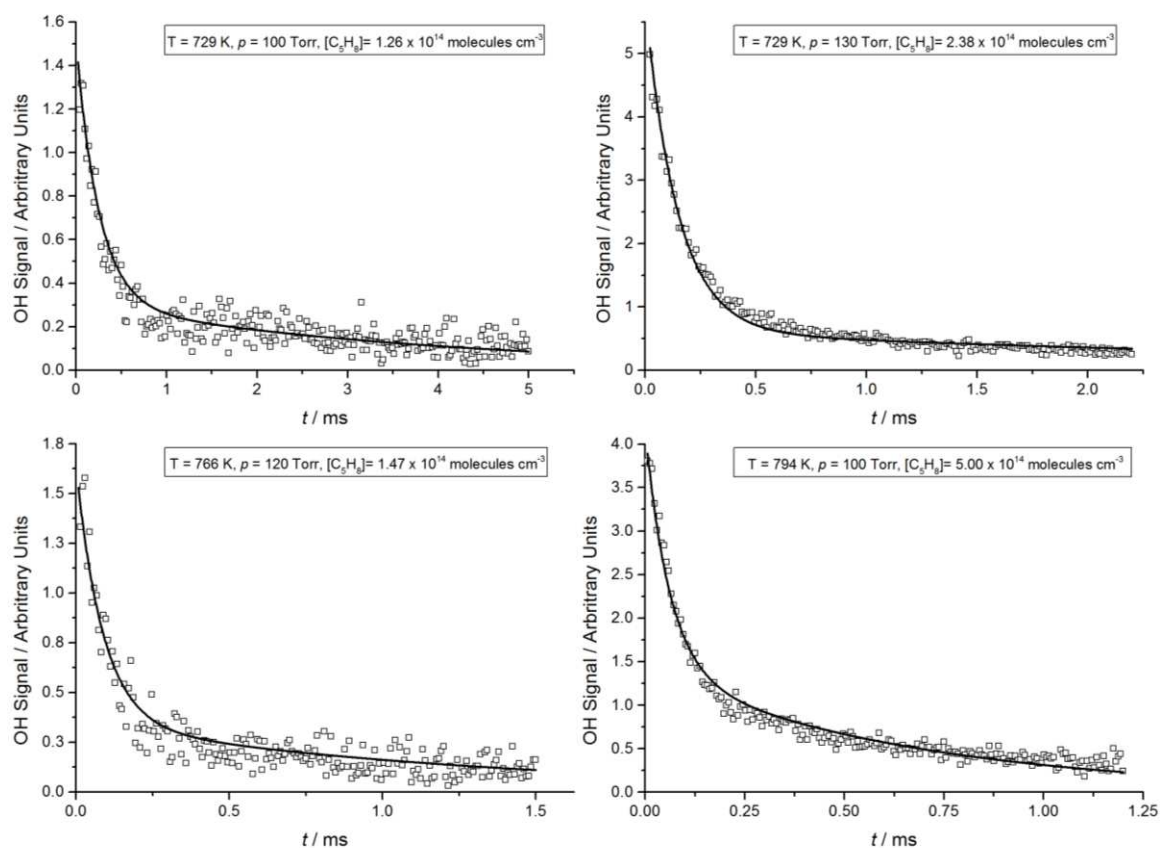


Figure 4. Examples of fits of non-exponential traces acquired at $T > 725$ K and $p \sim 100$ Torr.

4 Results and Discussion

4.1 Ab initio calculations

Figure 5 shows the potential energy surface for OH addition and H-abstraction from isoprene at the CCSD(T)/CBS//M06-2X/6-311++G(3df,2p) level. OH addition to C₂ or C₃ carbons produces adducts with significantly higher energies as there is no allylic stabilization of the resulting radicals. The energy difference between the C₁ and C₄ adducts is approximately 10 kJ mol⁻¹ (in good agreement with previous literature, see Table 3) and small compared to the total well depth. Whilst Table 3 shows that there is some variation in the absolute well-depths from various ab initio calculations, the energy difference between the two lowest energy adducts is very consistent at (10.1 ± 0.4) kJ mol⁻¹. In our subsequent MESMER analysis assessing the role of both adducts, the energy difference is fixed to our calculated value (10.1 kJ mol⁻¹), but the absolute well depth of the C₁ adduct is allowed to float. The barrier for the abstraction reaction is calculated to be 3.6 kJ mol⁻¹.

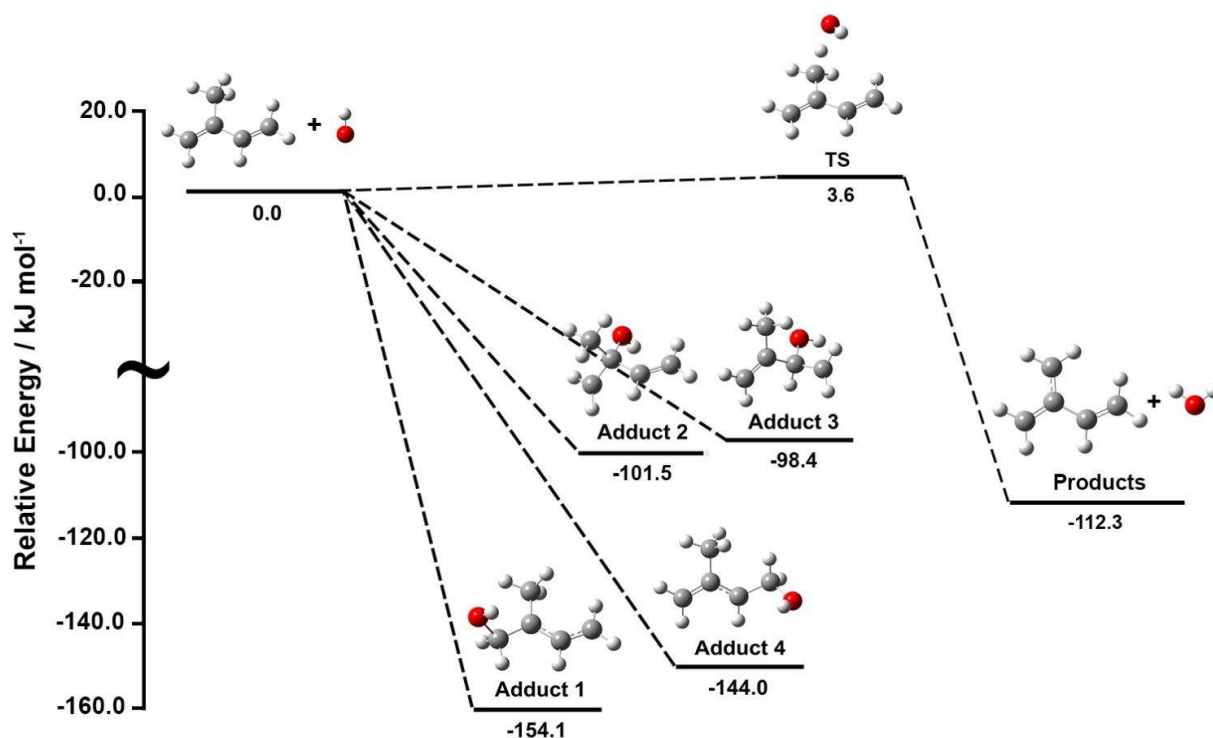


Figure 5. The potential energy diagram for the OH addition to isoprene. Relative energies were calculated at the CCSD(T)/CBS//M06-2X/6-311++G(3df,2p) level and include zero-point energy corrections.

Table 3. Theoretically calculated well-depths for the isoprene + OH reaction with respect to the additions at carbons 1 and 4. All well-depths are corrected for zero-point energies

Methodology	Reference	Well-depth adduct C ₁ / kJ mol ⁻¹	Well-depth adduct C ₄ / kJ mol ⁻¹	Energy Difference between adducts/ kJ mol ⁻¹
CCSD(T)/CBS//M06-2X/6-311++G(3df,2p)	This work	154.1	144.0	10.1
CCSD(T)/6-311G**//B3LYP/6-31G	Lei et al. ⁴⁶	145.6	135.1	10.5
roQCISD(T)/6-31++G**//B3LYP/6-311++G**	Greenwald et al. ⁴⁷	156.1 ^a	146.4	9.7
PMP4-(SDTQ)/6-311G**//MP2/6-311G**+ΔZPE/B3LYP/6-31G**	Stevens et al. ⁴⁸	158.6	148.1	10.5
CBS-APNO	Peeters et al. ¹⁴	163.2	153.6	9.6

a –including basis set correction at the roMP2 level of theory

The CCSD(T) method implemented in this work is known for accurately computing molecular properties and energies^{33, 38, 49} and is often referred to as “Gold Standard” of computational chemistry.⁵⁰ Our calculated well-depth differs from that obtained by Lei et al.⁴⁶ by 8.5 kJ mol⁻¹, who have implemented a similar methodology. The use of smaller basis sets for the calculations of single point energies and structural optimizations as a computational constraint (6-311G**⁵¹⁻⁵⁸ and 6-31G^{56, 59-67} respectively) contributes to the observed well-depth discrepancy. London dispersion forces which are accounted for at the M06-2X level, and neglected by the B3LYP⁶⁸⁻⁷¹ functional also contribute to the discrepancy.

Greenwald et al.⁴⁷, have applied the restricted open-shell quadratic configuration interaction (CI) technique, with perturbative triple excitations^{33, 72} to study the isomeric branching of the isoprene + OH reaction. In this correlated method, quadratic terms are included in the configuration coefficients to correct for size consistency. The authors have done a very careful study when obtaining the stationary structures of the four possible isoprene-OH adducts. They have located 58 different local minima for the adducts at the B3LYP/6-311++G** level, and implemented the lowest energy conformations in subsequent roQCISD(T) computations. The roQCISD(T)/6-31++G**//B3LYP/6-311++G** methodology was validated against previous calculations on the ethylene-OH case, where the well-depth was calculated to within ~3.35 kJ mol⁻¹.^{47, 73} They also report that the relative well-depths obtained at the PMP4(SDTQ)/6-311G**//B3LYP/6-311++G** level of theory are qualitatively aligned with those computed at the superior roQCISD(T)/6-31++G**//B3LYP/6-311++G** level.

Stevens et al.⁴⁸ have used the less computationally demanding fourth-order Møller-Plesset perturbation theory with single, double, triple and quadruple excitations and spin projection (PMP4(SDTQ)) to investigate the OH addition to isoprene. In the Møller-Plesset perturbation theory, the Hartree-Fock wavefunction is corrected for electron correlation by a

combination with configurational functions, originated from single, double, triple, etc. excitations.⁷⁴⁻⁷⁵ In their study, PMP4-(SDTQ)/6-311G** single point energies computed for MP2/6-311G** optimized structures were subsequently corrected with zero-point energies calculated at the B3LYP/6-31G** level. Their calculations show a well-depth only 2.51 kJ mol⁻¹ deeper than that reported by Greenwald et al.

Peeters et al. have employed the Complete basis set method CBS-APNO⁷⁶ to compute electronic energies while investigating the regeneration of HO_x in the oxidation of isoprene.¹⁴ The authors have verified that the CBS-APNO method systematically overestimated the well-depth of the CH₂=CH-ĊH₂ + O₂ and for this reason, a correction of 4.18 kJ mol⁻¹ have been applied. This fact suggests that the reported isoprene + OH well-depth might also be slightly overestimated by the CBS-APNO method.

4.2 Rate Coefficients for the OH + Isoprene Reaction, R1

Figure 2 shows an example of a typical experimental decay (inset) and bimolecular plot obtained at 406 K and 2 atm of nitrogen bath gas. Checks were carried out to ensure that the rate coefficients were invariant (within experimental error) of laser energy density (15 – 50 mJ cm⁻²) or repetition rate (1 – 10 Hz). Below 400 K, the addition of oxygen had no effect on the measured rate coefficient for reaction R1 as can be seen from Figure 2. Experiments in the presence of oxygen at temperatures > 450 K, where OH recycling was observed, will be presented in a subsequent publication focused on the validation of the LIM1 mechanism.¹⁵

A major issue when sampling the monitored species prior to detection, is whether the transit time from the sampling pinhole to detection influences the kinetic measurements.^{18, 77-79} In this study, room temperature pseudo-first-order rate coefficients of up to 70,000 s⁻¹ are in excellent agreement with the literature data. At higher first order rate coefficients, the influence of transport can be observed, but can potentially be accounted for with a biexponential analysis.⁷⁷ None of the measurements reported in this study required such corrections, i.e. transport is effectively instantaneous on the timescales of the chemical reaction. The analysis of the exponential decays is inset a few points to allow for the ~20 μs transport time.

Figure 6 illustrates the observed temperature dependence of k_1 from 298 – 794 K. In addition to varying the temperature, the pressure was also varied to ensure that measurements were always being made at the high pressure limit, i.e. that the observed bimolecular rate coefficients correspond to k_{1a}^{∞} . No evidence for any pressure dependence was observed from 50 – 1670 Torr for the 298 – 650 K temperature range and these observations were consistent with the modelling discussed in the subsequent sections. Measurements performed at $T \geq 725$ K are located in the fall-off region. For example, at 794 K, with $k_{1a, 794K} = (1.50 \pm 0.63) \times 10^{-11}$ cm³ molecule⁻¹ s⁻¹, our measurements are ~40% lower than our best estimate for k_{1a}^{∞} at that temperature (2.49×10^{-11} cm³ molecule⁻¹ s⁻¹). Excellent agreement is observed between the measurements performed with the high and low-pressure instruments, as evidenced by the proximity of the black and blue triangles in Figure 6.

A least-squares fit to the combined experimental data from both apparatus of the form $k_1^\infty = A \left(\frac{T}{298 \text{ K}}\right)^{-n}$ gives:

$$k_1^\infty = (10.4 \pm 0.4) \times 10^{-11} \left(\frac{T}{298 \text{ K}}\right)^{-1.34 \pm 0.12} \text{ cm}^3 \text{ molecule}^{-1} \text{ s}^{-1} \quad \text{E11}$$

where errors are at the 2σ level. The negative temperature dependence is consistent with previous literature and is dominated by the addition reaction; however, this work considerably extends the range of temperatures studied. A full discussion on the values of k_1 is presented in Section 4.5.

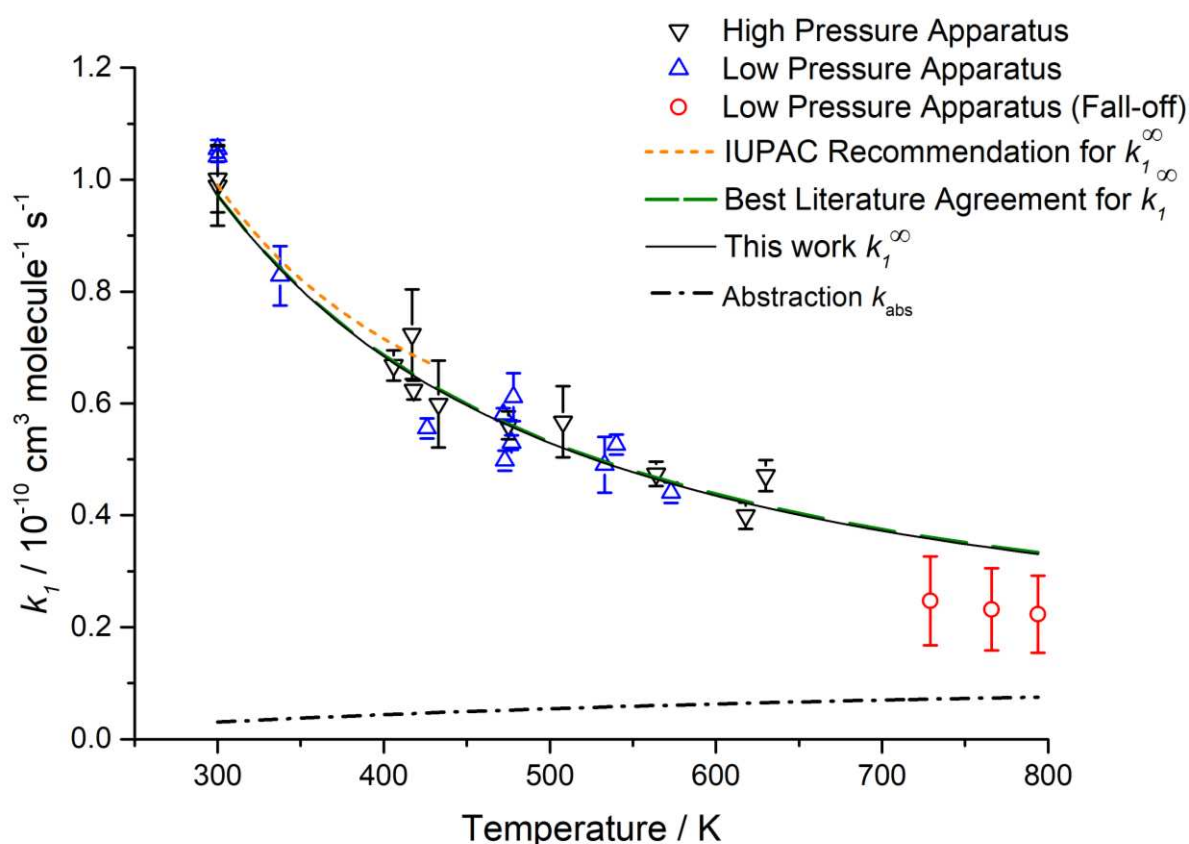


Figure 6. Comparison of experimental measurements using the high pressure instrument (black inverted triangles), measurements at the high pressure limit with a conventional low-pressure instrument (blue triangles) and at the fall-off region (red circles). The dotted line shows the IUPAC recommendation for the temperature dependence of the isoprene + OH reaction, the dashed line shows our best estimate for the high-pressure limit k_1^∞ , which was obtained from a ME from this work and selected data as discussed in part c of this section. The continuous line represents k_1^∞ as obtained based purely on our measurements. Errors are statistical at the 2σ level.

As can be seen from Table 4, the room temperature rate coefficients for reaction R1 are in excellent agreement with the IUPAC recommendation and the bulk of the experimental literature providing evidence that the new apparatus works well and can generate reliable rate coefficients.

Table 4. Comparison of Experimental Determinations of k_1

Author/date	Technique	Conditions	$10^{10}k_1/\text{cm}^3$ molecule ⁻¹ s ⁻¹ at 298 K	$k_1(\text{T})/\text{cm}^3$ molecule ⁻¹ s ⁻¹
This work	LFP ^a – high pressure OH detection	T = 298–630 K p = 1290–1670 Torr	0.99 ± 0.09	$(9.4 \pm 0.2) \times 10^{-11} \left(\frac{T}{298 \text{ K}}\right)^{-1.28 \pm 0.71} + (1.3 \pm 0.6) \times 10^{-11} \exp\left(\frac{-3.61 \text{ kJ mol}^{-1}}{RT}\right)$ ^b $(9.7 \pm 0.8) \times 10^{-11} \left(\frac{T}{298 \text{ K}}\right)^{-1.10 \pm 0.20}$ ^c $(2.0 \pm 0.2) \times 10^{-11} \exp\left(\frac{480 \pm 58}{T}\right)$ ^c
This work	LFP/LIF	T = 298–794 K p = 50–140 Torr	1.06 ± 0.02 (t-butOOH) 1.04 ± 0.02 (H ₂ O ₂)	$(9.6 \pm 0.2) \times 10^{-11} \left(\frac{T}{298 \text{ K}}\right)^{-1.39 \pm 0.56} + (1.3 \pm 0.6) \times 10^{-11} \exp\left(\frac{-3.61 \text{ kJ mol}^{-1}}{RT}\right)$ ^b $(10.5 \pm 0.4) \times 10^{-11} \left(\frac{T}{298 \text{ K}}\right)^{-1.38 \pm 0.12}$ ^{c*} $(1.8 \pm 0.1) \times 10^{-11} \exp\left(\frac{527 \pm 20}{T}\right)$ ^{c*}
This work	LFP/LIF ^d Combined data	T = 298–794 K p = 50–1670 Torr	n/a	$(9.5 \pm 1.2) \times 10^{-11} \left(\frac{T}{298 \text{ K}}\right)^{-1.33 \pm 0.32} + (1.3 \pm 0.6) \times 10^{-11} \exp\left(\frac{-3.61 \text{ kJ mol}^{-1}}{RT}\right)$ ^b $(10.4 \pm 0.4) \times 10^{-11} \left(\frac{T}{298 \text{ K}}\right)^{-1.34 \pm 0.12}$ ^{c*} $(1.8 \pm 0.2) \times 10^{-11} \exp\left(\frac{522 \pm 28}{T}\right)$ ^{c*}
IUPAC ³ (2013)	Review	n/a	1.00 ± 0.15	$2.7 \times 10^{-11} \exp(390 \pm 100/T)$
Atkinson and Aschmann ⁸⁰ (1984)	RR ^e	T = 295 K p = 760 Torr air	1.02 ± 0.04	
Atkinson et al. ⁸¹ (1982)	RR	T = 299 K p = 735 Torr air	1.00 ± 0.05	
Campuzano-Jost et al. ⁸² (2000)	LFP/LIF	T = 251–342 K p = 60–600 Torr	0.856 ± 0.026	$2.7 \times 10^{-11} \exp((336 \pm 74)/T)$
Campuzano-Jost et al. ⁸³ (2004)	LFP/LIF	T = 251–342 K p = 60–600 Torr	0.847 ± 0.059	$2.68 \times 10^{-11} \exp((348 \pm 136)/T)$
Chuong and Stevens ²¹ (2000)	DF ^f /LIF	T = 300–423 K p = 2–6 Torr He	1.10 ± 0.04	n/a

Chuong and Stevens (2002) ⁸⁴	DF/LIF	T = 300 K p = 100-150 Torr Ar	1.08 ± 0.05	
Dillon et al. ²² (2017)	LFP/LIF	T = 241–356 K p = 5–200 Torr (N ₂ or air)	0.93 ± 0.04	(1.93±0.08)×10 ⁻¹¹ exp((446±12)/T)
Edney et al. ⁸⁵ (1986)	RR	T = 297 K p = 1 atm air	1.01 ± 0.02	
Gill and Hites ⁸⁶ (2002)	RR	T = 298–363 K p = 1 atm He	1.01 ± 0.19	2.54×10 ⁻¹¹ exp((409±42)/T)
Hites and Turner ⁸⁷ (2009)	RR/MS ^g	T = 323–413 K p = 1 atm	n/a	4.0×10 ⁻¹¹ exp((249±20)/T)
Iida et al. ⁸⁸ (2002)	RR	T = 298 K p = 760 Torr air	1.04 ± 0.04	
Karl et al. ⁸⁹ (2004)	GC / LIF ^h	T = 294 K p = 760 Torr air	1.00 ± 0.12	
Kleindienst et al. ⁹⁰ (1982)	FP/RF	T = 297–23 K p = 50–200 Torr Ar	0.93 ± 0.15	2.36×10 ⁻¹¹ exp((409±28)/T)
McGivern et al. ¹⁹ (2000)	LFP/LIF	T = 295 K p = 0.5–20 Torr Ar	0.99 ± 0.05	
McQuaid et al. ⁹¹ (2002)	RR	T = 298 K p = 760 Torr air	1.11 ± 0.23	
Ohta ⁹² (1983)	RR	T = 297 K p = 760 Torr air	0.990 ± 0.027	
Park et al. ⁹³ (2004)	LFP/LIF	T = 279 – 336 K p = 1-8 Torr	1.08 ± 0.19	(3.49±0.46) ×10 ⁻¹¹ exp((366±40)/T)
Poppe et al. ⁹⁴ (2007)	LIF / MS / GC ^h	T = 295 K p = 760 Torr	1.02 ± 0.09	
Singh and Li ²⁰ (2007)	RR/DF/MS	T = 240 – 340 p = 1-3 Torr He	1.04 ± 0.19	2.3×10 ⁻¹¹ exp((444±27)/T)
Vimal et al. ⁹⁵ (2008)	DF / RF / LIF	T = 300 – 363 K p = 2 –5 Torr He	1.02 ± 0.06	
Zhang et al. ⁹⁶ (2001)	DF / MS	T = 298 K p = 1.9 Torr He	9.1	

Zhang et al. ⁹⁷ (2000)	DF / MS	T = 298 K p = 70–120 Torr N ₂	1.01 ± 0.08	
--------------------------------------	---------	---------------------------------------------	-------------	--

* – Measurements in the fall-off region (729 -794 K) were previously corrected to the high-pressure limit via Master Equation modelling. a – LFP = laser flash photolysis, b – Obtained from a Master Equation fit using the Trust region reflective algorithm⁹⁸, c – Obtained from a simple non-linear least squares fit, d – LIF = laser induced fluorescence, e – RR = relative rate methodology RF = Resonance fluorescence, f – DF = discharge flow, g – MS = mass spectrometric detection, h – Chamber study where rate coefficients were fitted with experimental modelling. Uncertainties reported at 2 σ for our data.

4.3 The Abstraction Channel R1b

From Figure 3, the fact that the green line fit (no abstraction) to the data is a much worse fit than the red line fit (with abstraction) is strong evidence that there is another loss process for OH in reaction R1. Abstraction is invoked to explain this behaviour as it has been observed in many other OH + alkene reactions and our calculations predict an abstraction barrier consistent with both our observations and those of other studies, see below. A good example is the reaction between OH and C₂H₄, where the abstraction becomes measurably significant above 650 K, and is characterized with a (24.9 ± 1.2) kJ mol⁻¹ barrier to abstraction.⁹⁹⁻¹⁰⁰ However, in the present system the barrier to H-abstraction at the CH₃ group is expected to be much lower as the electron delocalization of the resulting allylic radical, C₅H₇, leads to resonant stabilization, absent in the ethylene case.

The energy barrier of the allylic H abstraction from isoprene was theoretically explored with the aid of the Gaussian 09 D.01 software at the CCSD(T)/CBS//M06-2X/6-311++G(3df,2p) level of theory (see Figure 5). The calculated energetic barrier is equal to 3.6 kJ mol⁻¹, consistent with an allylic abstraction having a lower barrier than a vinylic abstraction. As evidenced from the red line fit to the data in Figure 3, incorporation of abstraction, k_{1b} , produces good fits to the experimental kinetic traces (also see global analysis traces, Figure 4). Abstraction reactions with barriers can be described using an Arrhenius description, and in the analysis of the equilibrium kinetic data - see Section 3.2 - the abstraction rate coefficient, k_{1b} , was modelled with equation E10. It was noted that over the temperature range of the experiments k_{1b} and E_{1b} were not uniquely pinpointed; many sets of Arrhenius parameters could reproduce k_{1b} . Therefore, in this data analysis E_{1b} was fixed to our theoretical value, 3.6 kJ mol⁻¹, and returned:

$$k_{1b} = (1.3 \pm 0.6) \times 10^{-11} \exp\left(\frac{-(3.6 \pm 3.5) \text{ kJ mol}^{-1}}{RT}\right) \text{ cm}^3 \text{ molecule}^{-1} \text{ s}^{-1}. \quad \text{E12}$$

This fixed value of E_{1b} provided the best fit to the data, but it is acknowledged other combinations of Arrhenius parameters can also provide an equally good fit to the data. As an exercise, E_{1b} was floated, but bounded very close to our calculated value, so that essentially, the value is unchanged. The returned uncertainty 3.5 kJ mol⁻¹ (2 σ) provides an estimate of how well E_{1b} is known. Using E12, k_1 can be divided up into k_{1a} and k_{1b} for all the temperatures carried out in this study. Summaries of k_{1a} and k_{1b} are given in the SI, in Tables S.1 and S.2.

While it is acknowledged that there are significant errors in extrapolating E12 to room temperature, the results suggest that $\sim 3 \pm 2\%$ of the R1 occurs via abstraction at 298 K, $k_{1b}(298 \text{ K}) = 3.1 \times 10^{-12} \text{ cm}^3 \text{ molecule}^{-1} \text{ s}^{-1}$. Atkinson et al. have predicted negligible hydrogen abstraction from the OH + isoprene reaction at room temperature, with an estimate for the upper limit of the branching ratio of 1%.¹⁰¹ However, the ability of previous experiments to observe abstraction were probably not any better than 5%, so our present estimate of $\sim 3\%$ does not contradict previous studies. We note that OH abstraction from 3-methyl-1-butene has been verified in a chamber study¹⁰² and product analysis reveals that the allylic H abstraction accounts for 5-10% of the overall OH reaction. Also, while no previous study has observed abstraction via R1, studies on the isoprene + Cl reaction indicate significant abstraction at room

temperature (~15%).¹⁰³⁻¹⁰⁴ The stable product of Cl abstraction at the CH₃ site, 2-methylene-3-butenal, was tentatively identified via atmospheric pressure ionization mass spectrometry.¹⁰³

In our high pressure apparatus, the total pressure is considerably greater than 1 atmosphere. This means that it is straightforward to exhaust the reaction gas mixture from our time-resolved experiments into the proton-transfer mass spectrometer, where the stable products can be analysed; the transfer time is a few seconds. The peak related to the mass of 2-methylene-3-butenal ($m/z = 83$) was monitored in the 298-473 K temperature range, in the presence of [O₂] ($> 1 \times 10^{18}$ molecule cm⁻³) to promote the oxidation of the potential allylic radical formed upon H abstraction. Figure 7 shows the variation of the $m/z = 83$ peak at room temperature, before and after the excimer laser is fired (5 Hz). Both the spectra were collected in the presence of H₂O₂, which means that when the laser is fired, the isoprene + OH chemistry is initiated. The observed promotion of peak $m/z = 83$ when the laser is fired corroborates the occurrence of abstraction via the allylic hydrogen. The promotion was also verified to be independent of isoprene concentration, which indicates that photolysis of isoprene is unlikely to be causing the observed effect.

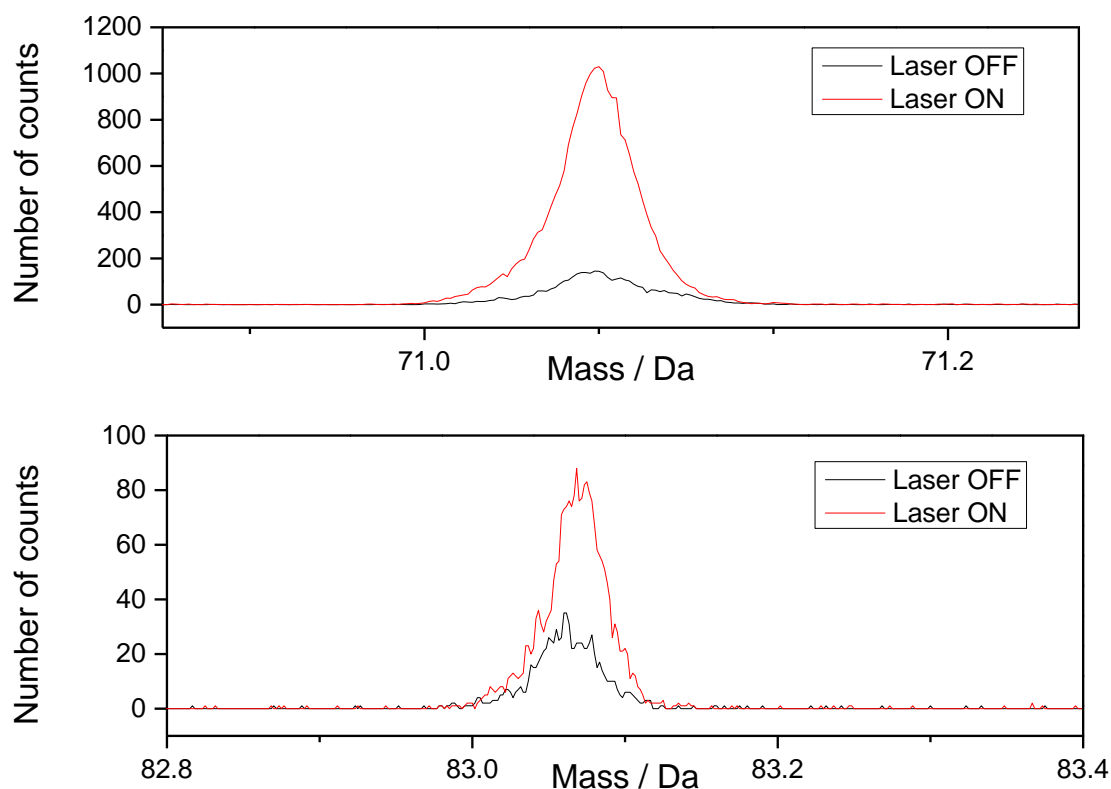


Figure 7. The change in the $m/z = 83$ at room temperature when the excimer laser is OFF (black line, no OH radicals generated) and ON (red line). [C₅H₈] = 5.3×10^{13} molecule cm⁻³, [O₂] = 1.2×10^{19} molecule cm⁻³, T = 298 K, p = 1200 Torr.

The stable products of the addition channel, R1a, in the presence of O₂ are expected to be methyl vinyl ketone and methacrolein, formed via HOC₅H₈O₂ self-reaction.¹⁰⁵ These products have identical mass and were observed with the proton-transfer mass spectrometer

($m/z = 71$) in much larger amounts compared to 2-methylene-3-butenal, see Figure 7. This result is evidence of direct abstraction, R1b, that is small, but not negligible at room temperature. The ratio of the peak areas ($a_{m/z = 83} / a_{m/z = 71}$) ~ 0.07 , is consistent with the reduced abstraction branching ratio if one assumes the molecules to have similar PTR-TOF-MS sensitivities.

4.4 Interpretation of OH + Isoprene \rightleftharpoons Adducts Equilibria

The isoprene molecule has four potential sites of OH addition as illustrated in Figure 5, however, a two-adduct model was adopted in the master equation (ME) calculations. Additions to the terminal carbons are believed to be dominant since they lead to the formation of stabilized allylic radicals.¹⁰⁶ Additions at C₁ and C₄, which account together for more than 90% of the total additions^{93,106} were therefore selected for implementation in our analysis. A ME calculation including the four possible additions reveals that the equilibrium fractions of the radicals generated from additions to carbons 2 and 3, together, account for less than 0.1% at 729 K. The significant equilibrium fractions of adducts 1 and 4 ($\sim 65\%$ and $\sim 35\%$ respectively) justifies that in our analysis only these two adducts are considered.

In the analysis of the experimental data, see Section 3.2, only one well was considered when determining the adduct dissociation rate coefficient, ($k_{-1a,expt}$). However, the current ME model considers two adducts (1 and 4). The two adduct model leads to tri-exponential OH decays, but to a very good approximation these decays can be modelled by a biexponential equation, and when fitted with equation E7, yields $k_{-1a,calc}$. In the analysis the parameters of the ME are adjusted in order that $k_{-1a,calc}$ best fits $k_{-1a,expt}$. This analysis means that both adducts are considered. Tests reveal that if the ME analysis had only considered adduct 1, the returned HOC₅H₈ binding energy would increase by approximately 2 kJ mol⁻¹.

The unimolecular coefficients $k_{-1a,expt}$ (see Table 2) were used to characterize the well-depths of the isoprene + OH reaction with the aid of the computational ME solver package MESMER⁴² and the numerical computing suite MATLAB R2016a¹⁰⁷ via the Trust Region Reflective Algorithm.⁹⁸ The logic is as follows: the ME was solved at the temperature and pressure of the experiments and generated an OH vs time profile, OH(t). This OH(t) was then passed to MATLAB where it is fitted to using equation E7, thus determining the calculated overall coefficient $k_{-1a,calc}$. The parameters of the ME - binding energy, energy transfer for each bath gas M ($A_{<\Delta E>d,M}$) and $k_1^\infty(T)$ were then adjusted by MATLAB in order to best fit $k_{-1a,calc}$ to $k_{-1a,expt}$, by minimizing the least-squares difference (χ^2). The results are given in Table 5. In this analysis the well-depths for adducts 1 and 4 were adjusted in unison, maintaining their constant 10.1 kJ mol⁻¹ difference, see Table 3. In the following discussion of the binding energy only adduct 1 is reported, as the energy of adduct 4 is simply 10.1 kJ mol⁻¹ higher.

Parameters obtained from a ME fit are dependent on the description of the molecular parameters (rotors, bends and vibrations) of the species involved in the reaction scheme. For example, the returned parameters are sensitive to the density of states of the reagents and adducts. This effect is evident when a vibration-only model is compared to a system where ten

small harmonic vibrational frequencies of the reactants and products ($\leq 350 \text{ cm}^{-1}$) are replaced by the hindered rotor approximation (See Figure 1). The returned well-depth for addition at carbon 1 when the hindered rotors are used, $(153.5 \pm 6.2) \text{ kJ mol}^{-1}$, is in excellent agreement with the theoretically calculated value at the CCSD(T)/CBS//M06-2X/6-311++G(3df,2p) level ($154.1 \text{ kJ mol}^{-1}$). However, the well-depth obtained with a less realistic vibration-only description of the system is significantly deeper, $(166.5 \pm 7.0) \text{ kJ mol}^{-1}$. Differences between our experimentally determined well-depth and theoretical values obtained at the different levels of theory presented range from 0.6 to 9.7 kJ mol^{-1} . Our best estimate of the binding energy, based purely on the measurements of this work is $(153.5 \pm 6.2) \text{ kJ mol}^{-1}$ and is given in Table 5.

Table 5. Comparison of Experimental and calculated k_{-1a} . Uncertainty at 1σ .

T / K	$k_{-1a,\text{expt}} / \text{s}^{-1}$	$k_{-1a,\text{calc}} / \text{s}^{-1}$	Adduct 1 Well-depth / kJ mol^{-1}
729	990 ± 870	1180	153.5 ± 6.2
766	3000 ± 2600	3160	
794	6500 ± 5500	6000	

The importance of the allylic hydrogen abstraction in the returned well-depths have also been explored in this investigation. If direct abstraction is neglected, then a unimolecular loss from the generic adduct presented in scheme S1 needs to be invoked (R3):



From Scheme S1, the solution is now given by $k_3 = k_{-1a} + k_R$, where the slope of the slow decay of the equilibrium traces, λ_- , is approximately equal to k_R . If the abstraction route is suppressed, i.e. $k_{1b} = 0$, k_R can provide an equally good fit to the data, but this reaction scheme skews k_{-1a} , which is the crucial parameter required to assign the binding energy of the adduct, $\text{C}_5\text{H}_8\text{-OH}$. For instance, at the highest temperature, 794 K, the value of k_{-1a} from Table 5 is $6500 \pm 5500 \text{ s}^{-1}$. However, if the highest temperature data are analysed with k_R , the returned value for k_{-1a} is $4810 \pm 4200 \text{ s}^{-1}$. This lower values of k_{-1a} increases the binding energy of the adduct by 3.8 kJ mol^{-1} . Even though we acknowledge that our experimental observations can be equally described using k_R , we do not have evidence for R8. Our theoretical calculations have identified the direct abstraction channel, R1b, see Figure 5. In addition, R3 predicts negligible abstraction at room temperature but R1b predicts 3%; our proton transfer mass spectrometer observes the abstraction product at room temperature, see Figure 7 and Section 4.3. Therefore, the direct abstraction channel, R1b, is the favoured explanation of the slow decay, λ_- .

Potential interference from radical-radical reactions ($\text{R} + \text{O}_2$ does not happen to any extent at these high temperatures) could also contribute to OH loss from the equilibrium system, but is considered unlikely using the following reasoning. The typical precursor concentration employed in the more sensitive equilibrium experiments ($\sim 1 \times 10^{14}$ molecule

cm^{-3} , calculated from OH removal in the absence of isoprene), the laser energy density ($\sim 15 \text{ mJ cm}^{-2}$ or $\sim 2 \times 10^{16}$ photons cm^{-2}), the precursor cross-section ($\sim 1 \times 10^{-19} \text{ cm}^2 \text{ molecule}^{-1}$ for H_2O_2) and the quantum yield, (2 for OH production from H_2O_2) is $\sim 4 \times 10^{11} \text{ molecule cm}^{-3}$. If $R + R$ is equal to $10^{-10} \text{ cm}^3 \text{ molecule}^{-1} \text{ s}^{-1}$ (upper limit) then this implies a $k_{1b} \sim 40 \text{ s}^{-1}$, which is much lower than experimentally observed k_{1b} . In some experiments with varying [OH] but similar $[\text{C}_5\text{H}_8]$ and temperature, no significant change in the kinetic parameters were observed. Additionally, at $T = 766 \text{ K}$ the photolysis wavelength was changed to 266 nm (fourth harmonic from Quantel, Q-smart laser, $\sim 10 \text{ mJ / pulse}$). Any minor photolysis of isoprene at 248 nm that could contribute to the radical pool and hence secondary chemistry, will be significantly reduced with this longer wavelength photolysis. The 266 nm data are wholly consistent with the other data, which is further evidence that little additional chemistry is occurring, other than that given by scheme S1.

4.5 Master Equation Modelling and Comparison with Literature

In this section the master equation modelling package MESMER, described previously, has been used to compare various experimental values of k_1 with a particular emphasis in determining the onset of pressure dependence. The complete data set of temperature and pressure dependent rate coefficients (187 values) from the references in Table 4 were fitted with the aid of MATLAB R2016a via the Trust Region Reflective Algorithm, in an analogous procedure to that described in the previous section. The only difference in the analysis that now MESMER also returns the forward isoprene + OH rate coefficients (k_{1a}) to MATLAB. A 10% uncertainty was assigned for all the rate coefficients considered in this analysis. The fitting parameters were: the adduct well depth, $A_{\langle \Delta E \rangle_{d,M}}$ for the relevant bath gases used, and the high pressure limiting values of $A_{1a, C1}$, $A_{1a, C4}$ and n in the same format as equation E8. The pre-exponential factors for additions to carbons 1 and 4 were linked to maintain their constant ratio ($A_{1a, C1} / A_{1a, C4} \sim 1.5$).¹⁹ The vibrational and rotational constants of isoprene and the OH- C_5H_8 adducts were calculated at the M06-2X/6-311++G(3df,2p) level of theory. Lennard Jones parameters were obtained from the work of Dibble et al.¹⁰⁸ and Lei et al.⁴⁶ A comparison of the complete experimental and fitted data is shown in Figure 8 and the resulting parameters are presented in Table 6.

The proximity of most data points to the $y = x$ line is expected from the IUPAC evaluation, where most studies are in excellent agreement. Three studies clearly stand out from the trend from this quantitative analysis; the low pressure measurements of Chuong and Stevens using discharge flow with OH detection by LIF, McGivern et al. using laser flash photolysis and LIF detection and the higher pressure LFP/LIF studies of Campuzano-Jost et al. Both of the low pressure measurements have been superseded by further, higher pressure measurements from the same research groups^{84, 93, 96} which are in good agreement with the IUPAC evaluation and the $y = x$ line of this comparison. However, other low pressure, discharge flow/LIF studies from Stevens' group, Vimal et al.⁹⁵, at 363 K point to some potentially interesting properties of the OH/isoprene system in comparison to OH/butadiene at low pressures. Over the pressure range of 1-6 Torr of helium at 363 K, the OH + isoprene

reaction is reported to show some pressure dependence (as does the study of Singh and Li under similar conditions), however, under identical conditions, the reactions of OH with the smaller butadiene and 1-butene molecules (which would be expected to demonstrate greater fall-off behaviour), show no pressure dependence. Vimal et al.⁹⁵ used molecular dynamics simulations to investigate whether differences in the mechanism of internal energy distribution in isoprene and 1,3-butadiene could explain the lack of pressure dependence in 1,3 butadiene. Although their calculations suggested differences in the mechanisms of IVR between the two compounds, they reported that further studies were required to identify whether such differences in IVR mechanisms could account for the varying pressure dependence. Our ME simulations suggest that at 363 K, the high-pressure limit should be reached at 0.4 Torr of He.

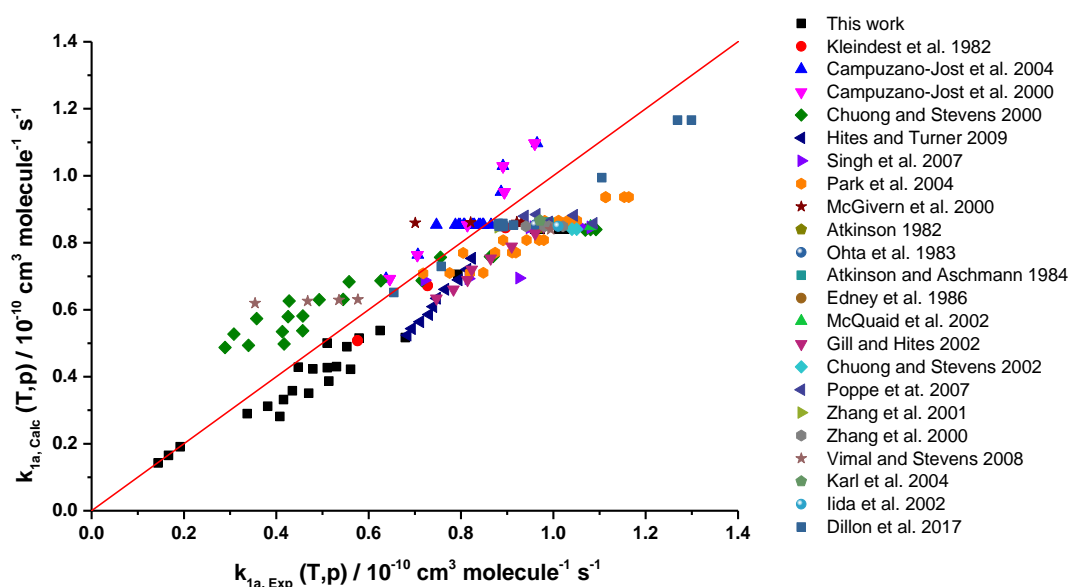


Figure 8. Correlation plot for experimental data points from all the data in Table 3 and the calculated rate coefficients generated by MESMER by allowing the well-depth, $A_{<\Delta E>d,M}$, A and n to be floated. The resulting parameters are shown in the second column of Table 6.

The work of Singh and Li²⁰ reports a pressure dependence of k_1 at 340 K over the 1 – 3 Torr pressure range of He. Their equivalent measurements of k_{1a}^{∞} at 1 and 2 Torr ($(7.21 \pm 0.65) \times 10^{-11}$ and $8.16 \times 10^{-11} \text{ cm}^3 \text{ molecule}^{-1} \text{ s}^{-1}$ respectively, corrected for abstraction with equation E12) are in good agreement with the set of selected studies presented previously, with ME predicted values of 7.92×10^{-11} and $7.98 \times 10^{-11} \text{ cm}^3 \text{ molecule}^{-1} \text{ s}^{-1}$ respectively. However, the rate coefficient measured at 3 Torr ($9.26 \times 10^{-11} \text{ cm}^3 \text{ molecule}^{-1} \text{ s}^{-1}$) is ~16% higher than what

our calculations predict ($8.00 \times 10^{-11} \text{ cm}^3 \text{ molecule}^{-1} \text{ s}^{-1}$). Our simulations suggest that, in helium at 340 K, the high-pressure limit should be reached at 0.2 Torr.

It is not easy to explain the discrepancy between the Campuzano-Jost et al.⁸²⁻⁸³ values and the remaining studies; Campuzano-Jost et al. recognised, but were unable to rationalize, the difference in their value of k_1 and other literature data. A number of checks were carried out by Campuzano-Jost et al. but they were unable to identify the origin of the discrepancy. Given the high value of the rate coefficient k_1 , it is very unlikely that radical-radical processes could influence the OH decays and the invariance of the rate coefficients with photolysis laser power suggests such secondary chemistry plays no role in OH decays. Rate coefficients lower than the expected value can be an indication of recycling reactions,¹⁰⁹⁻¹¹⁰ but the invariance of our measured rate coefficients at low temperatures with large concentrations of oxygen at least rules out oxygen leaks as a possible route to OH recycling in the Campuzano-Jost et al. experiments. Given the good agreement in the temperature dependence of k_1 with other measurements, the simplest explanation is some systematic error in determining isoprene concentrations in the reaction cell. That explanation is supported by the recent studies of Dillon et al.²² who determined UV absorption cross sections for isoprene which are approximately 10% greater than those of Campuzano-Jost et al. and in good agreement with another determination by Martins et al.¹¹¹ Dillon et al. re-evaluated the Campuzano-Jost data using their new cross sections, generally bringing the Campuzano-Jost et al. data in closer agreement to the IUPAC evaluation.

Removing the data sets from Campuzano-Jost et al., Chuong and Stevens, Vimal et al. and McGivern et al. produces a much better fit (as shown in Figure 9 and Table 6) with χ^2 being reduced from 601.34 (~3.22 per point) for the complete data set to 56.53 for the selected data set of 115 data points (~0.49 per point). $\chi^2 = 0.49$ implies that the data are on average within 6% of the fitted value. The resulting best fit parameters in the form of E8 are $A_{1a} = 9.52 \times 10^{-11} \text{ cm}^3 \text{ molecule}^{-1} \text{ s}^{-1}$ and $n_{1a}^\infty = -1.39$. Studies represented in Figure 9 are the preferred ones (including this work), and are referred to as ‘Selected Data’.

The returned parameters from the fittings where uncertainties were assigned as 10% of the measured coefficients are summarised in Table 6. It contains the returned parameters from considering the complete dataset and the selected data. While our k_{1a} data at high temperatures, where equilibria is observed, has much larger than 10% error, it is consistent with the selected data, under this 10% error criteria.

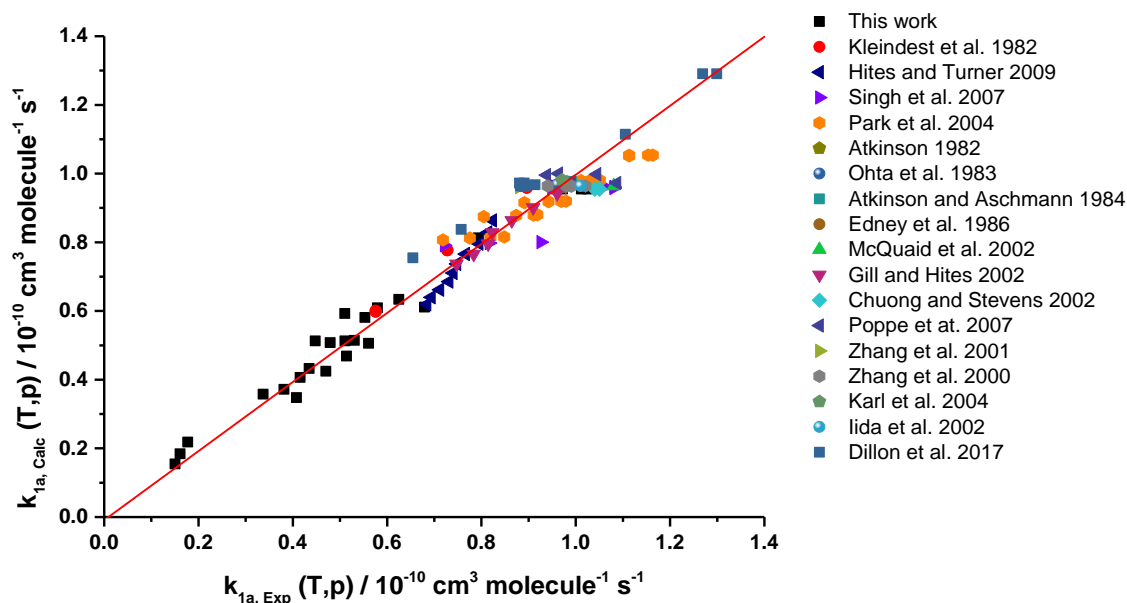


Figure 9. Correlation plot for experimental data points from selected data in Table 4 (see text) and the calculated rate coefficients generated by MESMER by allowing the well-depth, $A_{<\Delta E>d,M}$, A and n to be floated. The resulting parameters are shown in the ‘selected data’ column of Table 6.

The returned well-depth is virtually unaffected by which data are used as the well depth is almost exclusively determined by the high temperature data in this study. The other parameters associated with the fit: $A_{<\Delta E>d,M}$, A_{1a} and n_{1a} are more dependent on the data set used. For each dataset used, fitted parameters are reported with either all possibilities of $A_{<\Delta E>d,M}$ floated or with some fixed. Varying the degree of flexibility in fitting $A_{<\Delta E>d,M}$ makes little difference to the returned values of A and n^∞ ; these parameters are mainly dependent on the datasets considered in the analysis.

The analysis was also performed with the use of a single-adduct model; the results for this case are also included in Table 7. Little variation is observed in the returned parameters, with the well-depths varying by 2.5 kJ mol^{-1} . This small change is justified by the reduced equilibrium fraction of adduct 4 ($\sim 35\%$) compared to adduct 1 ($\sim 65\%$) and the small energetic difference to adduct 1 ($\sim 10 \text{ kJ mol}^{-1}$). Finally, the last three columns of Table 7 shows results, including uncertainties, obtained from fits where the selected data was incorporated, and the uncertainties of our high temperature measurements ($T > 720 \text{ K}$) were appropriately set as those of Table 2.

Table 6. Returned parameters from MESMER fits to this work and the literature data using a two-adduct model and accounting for H abstraction with all data given an equal uncertainty of 10%. $\langle \Delta E \rangle_{d,M} = A_{\langle \Delta E \rangle_{d,M}} \times (T/298)^{mc}$

	All Data			Selected Data		
Well depth, E/kJ mol ⁻¹	153.1	153.1	152.9	154.0	153.6	153.6
A _{<ΔE>d} / cm ⁻¹ He(m=1.00)	150 (Fixed)	150 (Fixed)	100	150 (Fixed)	150 (Fixed)	100
Ar (m=0.50)	250 (Fixed)	250 (Fixed)	250	250 (Fixed)	250 (Fixed)	100
N ₂ (m=0.25)	200 (Fixed)	200	190	200 (Fixed)	150	150
A × 10 ¹¹ / cm ³ molecule ⁻¹ s ⁻¹	8.32	8.33	8.34	9.55	9.52	9.52
n [∞]	-1.45	-1.45	-1.45	-1.44	-1.39	-1.39
χ ² per point	3.31	3.31	3.22	0.56	0.49	0.49

Table 7. Returned parameters from MESMER fits to this work and the literature data and accounting for H abstraction with our higher temperature data given the uncertainties reported in Table 2. $\langle \Delta E \rangle_{d,M} = A_{\langle \Delta E \rangle_{d,M}} \times (T/298)^m$

	This work Two adduct model		This work One adduct model (C ₁)		Selected Data		
Well depth, E/kJ mol ⁻¹	153.7 ± 5.9	153.5 ± 6.2	156.0 ± 3.9	156.0 ± 4.2	153.6 ± 4.9	153.4 ± 5.1	153.2 ± 5.0
A _{<ΔE>d} / cm ⁻¹ He(m=1.00)	n/a	n/a	n/a	n/a	150 (Fixed)	150 (Fixed)	100 ± 350
Ar (m=0.50)	n/a	n/a	n/a	n/a	250 (Fixed)	250 (Fixed)	100 ± 340
N ₂ (m=0.25)	200 (Fixed)	150 ± 110	200 (Fixed)	150 ± 70	200 (Fixed)	150 ± 90	150 ± 90
A × 10 ¹¹ / cm ³ molecule ⁻¹ s ⁻¹	9.53 ± 0.64	9.47 ± 0.65	9.46 ± 0.41	9.46 ± 0.42	9.46 ± 0.14	9.46 ± 0.14	9.47 ± 0.16
n [∞]	-1.35 ± 0.15	-1.33 ± 0.16	-1.33 ± 0.10	-1.32 ± 0.10	-1.34 ± 0.07	-1.33 ± 0.07	-1.33 ± 0.07
χ ² per point	0.50	0.48	0.49	0.48	0.42	0.41	0.41

4.6 Analytical Representation of Pressure and Temperature for k_{1a} , $k_{-1a,C1}$, and $k_{-1a,C4}$

In order to provide analytical representations for the present master equation calculations, the output from our MESMER equations have been fitted using a Troe formalism:

$$k_{1a}(T,[M]) = \frac{k_{1a,0}(T)[M]}{1 + \frac{k_{1a,0}(T)[M]}{k_{1a}^{\infty}(T)}} F(x) \quad \text{E13}$$

$$k_{-1a,C1}(T,[M]) = k_{1a}(T,[M]) \times (RT)^{-1} \times \exp(\Delta H_{C1}^{\ominus}/RT) \times \exp(-\Delta S_{C1}^{\ominus}/R) \quad \text{E14}$$

$$k_{-1a,C4}(T,[M]) = k_{1a}(T,[M]) \times (RT)^{-1} \times \exp(\Delta H_{C4}^{\ominus}/RT) \times \exp(-\Delta S_{C4}^{\ominus}/R) \quad \text{E15}$$

where $[M]$ is the concentration of the buffer gas, $k_{1a,0}(T)$ is the low-pressure termolecular rate coefficient, $k_{1a}^{\infty}(T)$ is the high-pressure limit rate coefficient, and $F(x)$ is the collision broadening factor. The collision broadening factor - $F(x)$ - is calculated according to the formulation of Troe and Ushakov¹¹², see Supporting Information. $k_{-1a,C1}$ and $k_{-1a,C4}$ are the decomposition rate coefficients for adducts 1 and 4, respectively, and are related to k_{1a} via E14 and E15 using their thermodynamic parameters: ΔH_{C1} , ΔS_{C1} and ΔH_{C4} , ΔS_{C4} .

A global non-linear least-squares fit to the MESMER data using the Troe formalism was carried out, where $k_0(T)$ and $k_{1a}^{\infty}(T)$ were defined according to equations E8a and E8b respectively.

$$k_0(T) = A_0 \times (T/298)^n \text{ cm}^6 \text{ molecule}^{-2} \text{ s}^{-1} \quad \text{E8a}$$

$$k_{1a}^{\infty}(T) = A_{1a} \times (T/298)^m \text{ cm}^3 \text{ molecule}^{-1} \text{ s}^{-1} \quad \text{E8b}$$

A_0 , A_{1a} , n and m , and $F(x)$ (F_{centA} , F_{centB} , x_0 and b), $\Delta H_{C1,C4}$, $\Delta S_{C1,C4}$ were adjusted to provide a good fit to the simulated pressure dependent coefficients $k_{1a}(T,[M])$. The results are given in Table 8, and these fits to the MESMER data are shown in Figure 10, where N_2 was defined as the bath gas. Additional Troe fits where helium and argon were simulated as the buffer gases are also given in Table 8.

Table 8. Troe fit parameters to MESMER-simulated rate coefficients, for N_2 , He, Ar.

	N_2	He	Ar
$A_{1a} / 10^{-11} \text{ cm}^3 \text{ molecule}^{-1} \text{ s}^{-1}$	9.5	9.6	9.5
n	-1.26	-1.30	-1.30
$A_0 / 10^{-21} \text{ cm}^6 \text{ molecule}^{-2} \text{ s}^{-1}$	1.68	1.10	1.43
m	-14.08	-12.50	-13.27
b	0.08	0.08	0.08
x_0	0.90	0.88	0.90
F_{centA}	0.10	0.11	0.13
F_{centB}	-0.0012	-0.0012	-0.0009
$\Delta H_{C1}^{\ominus} / \text{J mol}^{-1}$	154043	154308	154512
$\Delta S_{C1}^{\ominus} / \text{J mol}^{-1} \text{ K}^{-1}$	108.9	109.3	109.6
$\Delta H_{C4}^{\ominus} / \text{J mol}^{-1}$	147251	147495	147696
$\Delta S_{C4}^{\ominus} / \text{J mol}^{-1} \text{ K}^{-1}$	102.8	103.1	103.5

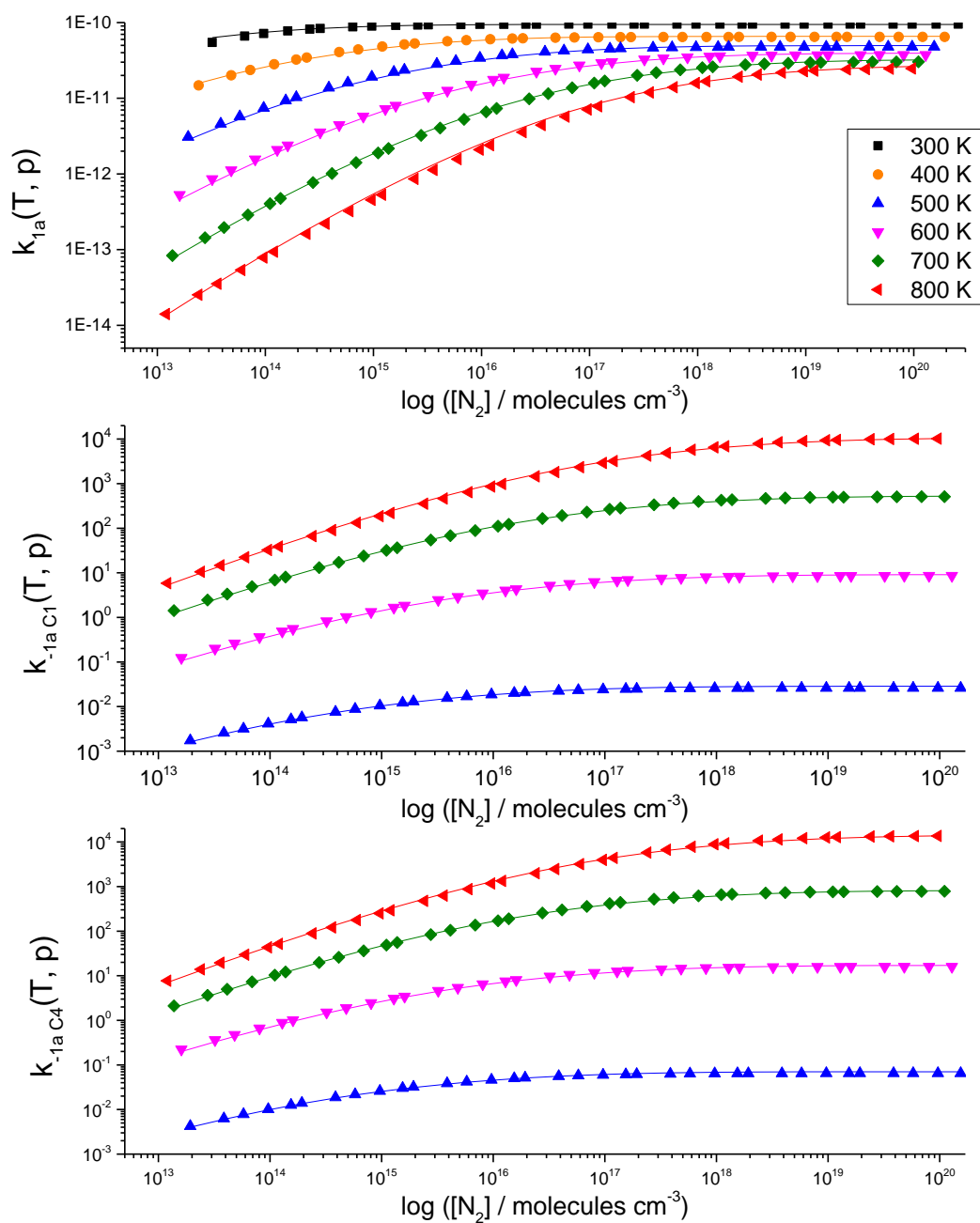


Figure 10. Fits of the Troe formalism to MESMER-simulated rate coefficients where N_2 was implemented as the buffer gas at various temperatures. Markers represent MESMER-simulated rate coefficients and the lines of the same colour are the Troe fits to the data.

5 Summary and Conclusions

Measurements of the rate coefficient for the reaction of OH with isoprene, k_1 , made around room temperature using a new apparatus for high pressure studies are in good agreement with the extensive literature data, hence validating this new apparatus.

Above ~ 700 K the OH temporal profiles exhibit biexponential behaviour, consistent with the establishment of the $\text{OH} + \text{C}_5\text{H}_8 \rightleftharpoons$ adduct equilibrium. The experimental adduct dissociation data, k_{-1a} , were fitted to using a master equation model where the adduct binding energy was adjusted. This analysis determined a well depth of (153.5 ± 6.2) kJ mol^{-1} for adduct 1, C1, and (143.4 ± 6.2) kJ mol^{-1} for adduct 4, C4. This value is in agreement with the present ab initio calculations (well depth for C1 adduct = 154.1 kJ mol^{-1}) on the R1 potential energy surface. However, it is noted that the well depth determined from the experimental data is dependent on how the internal modes of reagents and adducts are treated, and only when the low vibrations are treated as hindered rotor does experiment and theory show agreement.

The analysis of the > 700 K equilibrium data required an additional minor, but significant abstraction channel, R1b. Our ab initio calculations have identified this direct abstraction channel and the proton transfer mass spectrometer provides evidence that this channel is operating even at room temperature: $k_{1b} = (1.3 \pm 0.3) \times 10^{-11} \exp\left(\frac{-3.61 \text{ kJ mol}^{-1}}{RT}\right) \text{ cm}^3 \text{ molecule}^{-1} \text{ s}^{-1}$.

Our experimental data on reaction k_1 , together with the extensive literature data on this reaction, have been assessed using master equation analysis with the MESMER programme. This analysis indicates that there is no pressure dependence in the pressure range of the literature data, contradicting some previous studies. A selected dataset was then used to provide our recommended value for $k_{1a}(T, [M])$. A Troe parametrization of $k_{1a}(T, [M])$ provides an analytical form of our MESMER analysis. The temperature range for OH + isoprene studies has been significantly extended to ~ 800 K with $k_1^\infty = (9.5 \pm 0.2) \times 10^{-11} \left(\frac{T}{298 \text{ K}}\right)^{-1.33 \pm 0.07} + (1.3 \pm 0.3) \times 10^{-11} \exp\left(\frac{-3.61 \text{ kJ mol}^{-1}}{RT}\right)$.

Supporting Information

Electronic supporting information is available containing experimental data, frequencies and structures from ab initio calculations, recommended partitioning between addition and abstraction as a function of temperature, Troe fits with He and Ar as third body, MESMER and Origin Scripts.

Acknowledgements

The authors are grateful to the Brazilian National Council for Scientific and Technological Development (CNPq, grant reference number 206527/2014-4) for support for DJM, to NERC for a studentship for THS and to NCAS.

References

1. Hantson, S.; Knorr, W.; Schurgers, G.; Pugh, T. A. M.; Arneth, A. Global Isoprene and Monoterpene Emissions under Changing Climate, Vegetation, CO₂ and Land Use. *Atmos. Environ.* **2017**, *155*, 35-45.
2. Guenther, A.; Karl, T.; Harley, P.; Wiedinmyer, C.; Palmer, P. I.; Geron, C. Estimates of Global Terrestrial Isoprene Emissions Using Megan (Model of Emissions of Gases and Aerosols from Nature). *Atmos. Chem. Phys.* **2006**, *6*, 3181-3210.
3. IUPAC Evaluated Kinetic Data. <http://iupac.pole-ether.fr/index.html> (accessed February).
4. Utembe, S. R.; Jenkin, M. E.; Derwent, R. G.; Lewis, A. C.; Hopkins, J. R.; Hamilton, J. F. Modelling the Ambient Distribution of Organic Compounds During the August 2003 Ozone Episode in the Southern Uk. *Faraday Discuss.* **2005**, *130*, 311-326.
5. Tan, D. et al. HOx Budgets in a Deciduous Forest: Results from the Prophet Summer 1998 Campaign. *J. Geophys. Res. Atmos.* **2001**, *106*, 24407-24427.
6. Carslaw, N. et al. OH and HO₂ Radical Chemistry in a Forested Region of North-Western Greece. *Atmos. Environ.* **2001**, *35*, 4725-4737.
7. Whalley, L. K. et al. Quantifying the Magnitude of a Missing Hydroxyl Radical Source in a Tropical Rainforest. *Atmos. Chem. Phys.* **2011**, *11*, 7223-7233.
8. Lelieveld, J. et al. Atmospheric Oxidation Capacity Sustained by a Tropical Forest. *Nature.* **2008**, *452*, 737-740.
9. Saunio, M. et al. The Global Methane Budget 2000-2012. *ESSD.* **2016**, *8*, 697-751.
10. Seakins, P. W.; Blitz, M. A., Developments in Laboratory Studies of Gas-Phase Reactions for Atmospheric Chemistry with Applications to Isoprene Oxidation and Carbonyl Chemistry. In *Annual Review of Physical Chemistry, Vol 62*, Leone, S. R.; Cremer, P. S.; Groves, J. T.; Johnson, M. A., Eds. Annual Reviews: Palo Alto, 2011; Vol. 62, pp 351-373.
11. Winiberg, F. A. F. et al. Direct Measurements of OH and Other Product Yields from the HO₂ + CH₃C(O)O₂ Reaction. *Atmos. Chem. Phys.* **2016**, *16*, 4023-4042.
12. Hansen, R. F.; Lewis, T. R.; Graham, L.; Whalley, L. K.; Seakins, P. W.; Heard, D. E.; Blitz, M. A. OH Production from the Photolysis of Isoprene-Derived Peroxy Radicals: Cross-Sections, Quantum Yields and Atmospheric Implications. *Phys. Chem. Chem. Phys.* **2017**, *19*, 2341-2354.
13. Paulot, R.; Crouse, J. D.; Kjaergaard, H. G.; Kurten, A.; St. Clair, J. M.; Seinfeld, J. H.; Wennberg, P. O. Unexpected Epoxide Formation in the Gas-Phase Photooxidation of Isoprene. *Science.* **2009**, *325*, 730 - 733.
14. Peeters, J.; Nguyen, T. L.; Vereecken, L. HOx Radical Regeneration in the Oxidation of Isoprene. *Phys. Chem. Chem. Phys.* **2009**, *11*, 5935-5939.
15. Peeters, J.; Muller, J. F.; Stavrou, T.; Nguyen, V. S. Hydroxyl Radical Recycling in Isoprene Oxidation Driven by Hydrogen Bonding and Hydrogen Tunneling: The Upgraded Lim1 Mechanism. *J. Phys. Chem. A* **2014**, *118*, 8625-8643.
16. Seakins, P. W. A Brief Review of the Use of Environmental Chambers for Gas Phase Studies of Kinetics, Chemical Mechanisms and Characterisation of Field Instruments. *EPJ Web Conf.* **2010**, *9*, 143-163.
17. Eskola, A. J.; Carr, S. A.; Shannon, R. J.; Wang, B.; Blitz, M. A.; Pilling, M. J.; Seakins, P. W.; Robertson, S. H. Analysis of the Kinetics and Yields of OH Radical Production from the CH₃OCH₂ + O₂ Reaction in the Temperature Range 195-650 K: An Experimental and Computational Study. *J. Phys. Chem. A* **2014**, *118*, 6773-6788.
18. Stone, D.; Blitz, M.; Ingham, T.; Onel, L.; Medeiros, D. J.; Seakins, P. W. An Instrument to Measure Fast Gas Phase Radical Kinetics at High Temperatures and Pressures. *Rev. Sci. Instrum.* **2016**, *87*, 054102.
19. McGivern, W. S.; Suh, I.; Clinkenbeard, A. D.; Zhang, R. Y.; North, S. W. Experimental and Computational Study of the OH-Isoprene Reaction: Isomeric Branching and Low-Pressure Behavior. *J. Phys. Chem. A* **2000**, *104*, 6609-6616.

20. Singh, S.; Li, Z. Kinetics Investigation of OH Reaction with Isoprene at 240-340 K and 1-3 Torr Using the Relative Rate/Discharge Flow/Mass Spectrometry Technique. *J. Phys. Chem. A* **2007**, *111*, 11843-11851.
21. Chuong, B.; Stevens, P. S. Kinetic Study of the OH Plus Isoprene and OH Plus Ethylene Reactions between 2 and 6 Torr and over the Temperature Range 300-423 K. *J. Phys. Chem. A* **2000**, *104*, 5230-5237.
22. Dillon, T. J.; Dulitz, K.; Gross, C. B. M.; Crowley, J. N. Temperature Dependent Rate Coefficients for the Reactions of the Hydroxyl Radical with the Atmospheric Biogenics Isoprene, alpha-pinene and delta-3-carene. *Atmos. Chem. Phys.* **2017**, *17*, 15137-15150
23. Blitz, M. A.; Green, N. J. B.; Shannon, R. J.; Pilling, M. J.; Seakins, P. W.; Western, C. M.; Robertson, S. H. Reanalysis of Rate Data for the Reaction $\text{CH}_3 + \text{CH}_3 \rightarrow \text{C}_2\text{H}_6$ Using Revised Cross Sections and a Linearized Second-Order Master Equation. *J. Phys. Chem. A* **2015**, *119*, 7668-7682.
24. Atkinson, R.; Baulch, D. L.; Cox, R. A.; Crowley, J. N.; Hampson, R. F.; Hynes, R. G.; Jenkin, M. E.; Rossi, M. J.; Troe, J. Evaluated Kinetic and Photochemical Data for Atmospheric Chemistry: Volume I - Gas Phase Reactions of Ox, HOx, NOx and SOx Species. *Atmos. Chem. Phys.* **2004**, *4*, 1461-1738.
25. Onel, L.; Blitz, M. A.; Breen, J.; Rickardcd, A. R.; Seakins, P. W. Branching Ratios for the Reactions of OH with Ethanol Amines Used in Carbon Capture and the Potential Impact on Carcinogen Formation in the Emission Plume from a Carbon Capture Plant. *Phys. Chem. Chem. Phys.* **2015**, *17*, 25342-25353.
26. Onel, L.; Blitz, M. A.; Seakins, P. W. A Laser Flash Photolysis, Laser Induced Fluorescence Determination of the Rate Coefficient for the Reaction of OH Radicals with Monoethanol Amine (Mea) from 296 - 510 K. *J. Phys. Chem. Lett.* **2012**, *3*, 853-856.
27. Seakins, P. W.; Pilling, M. J.; Niiranen, J. T.; Gutman, D.; Krasnoperov, L. N. Kinetics and Thermochemistry of $\text{R} + \text{HBr} = \text{RH} + \text{Br}$ Reactions - Determinations of the Heat of Formation of C_2H_5 , $i\text{-C}_3\text{H}_7$, $\text{sec-C}_4\text{H}_9$, and $t\text{-C}_4\text{H}_9$. *J. Phys. Chem.* **1992**, *96*, 9847-9855.
28. Zhao, Y.; Truhlar, D. G. The M06 Suite of Density Functionals for Main Group Thermochemistry, Thermochemical Kinetics, Noncovalent Interactions, Excited States, and Transition Elements: Two New Functionals and Systematic Testing of Four M06-Class Functionals and 12 Other Functionals. *Theor. Chem. Acc.* **2008**, *120*, 215-241.
29. Frisch, M. J.; Pople, J. A.; Binkley, J. S. Self-Consistent Molecular-Orbital Methods .25. Supplementary Functions for Gaussian-Basis Sets. *J. Chem. Phys.* **1984**, *80*, 3265-3269.
30. Frisch, M. J. et al., Gaussian 09, Revision D.01. Wallingford CT, 2009.
31. Peng, C. Y.; Ayala, P. Y.; Schlegel, H. B.; Frisch, M. J. Using Redundant Internal Coordinates to Optimize Equilibrium Geometries and Transition States. *J. Comput. Chem.* **1996**, *17*, 49-56.
32. Li, X. S.; Frisch, M. J. Energy-Represented Direct Inversion in the Iterative Subspace within a Hybrid Geometry Optimization Method. *J. Chem. Theory Comput.* **2006**, *2*, 835-839.
33. Raghavachari, K.; Trucks, G. W.; Pople, J. A.; Headgordon, M. A 5th-Order Perturbation Comparison of Electron Correlation Theories. *Chem. Phys. Lett.* **1989**, *157*, 479-483.
34. Helgaker, T.; Klopper, W.; Koch, H.; Noga, J. Basis-Set Convergence of Correlated Calculations on Water. *J. Chem. Phys.* **1997**, *106*, 9639-9646.
35. Papajak, E.; Zheng, J.; Xu, X.; Leverentz, H. R.; Truhlar, D. G. Perspectives on Basis Sets Beautiful: Seasonal Plantings of Diffuse Basis Functions. *J. Chem. Theory Comput.* **2011**, *7*, 3027-3034.
36. Kendall, R. A.; Dunning, T. H.; Harrison, R. J. Electron-Affinities of the 1st-Row Atoms Revisited - Systematic Basis-Sets and Wave-Functions. *J. Chem. Phys.* **1992**, *96*, 6796-6806.
37. Feller, D. The Use of Systematic Sequences of Wave-Functions for Estimating the Complete Basis Set, Full Configuration-Interaction Limit in Water. *J. Chem. Phys.* **1993**, *98*, 7059-7071.
38. Ramabhadran, R. O.; Raghavachari, K. Extrapolation to the Gold-Standard in Quantum Chemistry: Computationally Efficient and Accurate CCSD(T) Energies for Large Molecules Using an Automated Thermochemical Hierarchy. *J. Chem. Theory Comput.* **2013**, *9*, 3986-3994.

39. Liu, Z.; Nguyen, V. S.; Harvey, J.; Muller, J. F.; Peeters, J. Theoretically Derived Mechanisms of HpalD Photolysis in Isoprene Oxidation. *Phys. Chem. Chem. Phys.* **2017**, *19*, 9096-9106.
40. Alecu, I. M.; Zheng, J.; Zhao, Y.; Truhlar, D. G. Computational Thermochemistry: Scale Factor Databases and Scale Factors for Vibrational Frequencies Obtained from Electronic Model Chemistries. *J. Chem. Theory Comput.* **2010**, *6*, 2872-2887.
41. Sharma, S.; Raman, S.; Green, W. H. Intramolecular Hydrogen Migration in Alkylperoxy and Hydroperoxyalkylperoxy Radicals: Accurate Treatment of Hindered Rotors. *J. Phys. Chem. A* **2010**, *114*, 5689-5701.
42. Glowacki, D. R.; Liang, C. H.; Morley, C.; Pilling, M. J.; Robertson, S. H. Mesmer: An Open-Source Master Equation Solver for Multi-Energy Well Reactions. *J. Phys. Chem. A* **2012**, *116*, 9545-9560.
43. Pilling, M. J.; Robertson, S. H. Master Equation Models for Chemical Reactions of Importance in Combustion. *Annu. Rev. Phys. Chem.* **2003**, *54*, 245-275.
44. Bartis, J. T.; Widom, B. Stochastic-Models of Interconversion of 3 or More Chemical Species. *J. Chem. Phys.* **1974**, *60*, 3474-3482.
45. OriginLab *Originpro*, Northampton, MA.
46. Lei, W. F.; Zhang, R. Y.; McGivern, W. S.; Derecskei-Kovacs, A.; North, S. W. Theoretical Study of Isomeric Branching in the Isoprene-OH Reaction: Implications to Final Product Yields in Isoprene Oxidation. *Chem. Phys. Lett.* **2000**, *326*, 109-114.
47. Greenwald, E. E.; North, S. W.; Georgievskii, Y.; Klippenstein, S. J. A Two Transition State Model for Radical-Molecule Reactions: Applications to Isomeric Branching in the OH-Isoprene Reaction. *J. Phys. Chem. A* **2007**, *111*, 5582-5592.
48. Stevens, P. S.; Seymour, E.; Li, Z. J. Theoretical and Experimental Studies of the Reaction of OH with Isoprene. *J. Phys. Chem. A* **2000**, *104*, 5989-5997.
49. Řezáč, J.; Šimová, L.; Hobza, P. CCSD[T] Describes Noncovalent Interactions Better Than the CCSD(T), CCSD(TQ), and CCSDT Methods. *J. Chem. Theory Comput.* **2013**, *9*, 364-369.
50. Řezáč, J.; Hobza, P. Describing Noncovalent Interactions Beyond the Common Approximations: How Accurate Is the "Gold Standard," CCSD(T) at the Complete Basis Set Limit? *J. Chem. Theory Comput.* **2013**, *9*, 2151-2155.
51. Wachters, A. J. H. Gaussian Basis Set for Molecular Wavefunctions Containing Third-Row Atoms. *J. Chem. Phys.* **1970**, *52*, 1033-1036.
52. Hay, P. J. Gaussian Basis Sets for Molecular Calculations. The Representation of 3d Orbitals in Transition-Metal Atoms. *J. Chem. Phys.* **1977**, *66*, 4377-4384.
53. Krishnan, R.; Binkley, J. S.; Seeger, R.; Pople, J. A. Self-Consistent Molecular Orbital Methods. XX. A Basis Set for Correlated Wave Functions. *J. Chem. Phys.* **1980**, *72*, 650-654.
54. McLean, A. D.; Chandler, G. S. Contracted Gaussian Basis Sets for Molecular Calculations. I. Second Row Atoms, Z=11-18. *J. Chem. Phys.* **1980**, *72*, 5639-5648.
55. Raghavachari, K.; Trucks, G. W. Highly Correlated Systems. Excitation Energies of First Row Transition Metals Sc-Cu. *J. Chem. Phys.* **1989**, *91*, 1062-1065.
56. Binning, R. C.; Curtiss, L. A. Compact Contracted Basis Sets for Third-Row Atoms: Ga-Kr. *J. Comput. Chem.* **1990**, *11*, 1206-1216.
57. McGrath, M. P.; Radom, L. Extension of Gaussian-1 (G1) Theory to Bromine-Containing Molecules. *J. Chem. Phys.* **1991**, *94*, 511-516.
58. Curtiss, L. A.; McGrath, M. P.; Blaudeau, J. P.; Davis, N. E.; Jr., R. C. B.; Radom, L. Extension of Gaussian-2 Theory to Molecules Containing Third-Row Atoms Ga-Kr. *J. Chem. Phys.* **1995**, *103*, 6104-6113.
59. Rassolov, V. A.; Ratner, M. A.; Pople, J. A.; Redfern, P. C.; Curtiss, L. A. 6-31g* Basis Set for Third-Row Atoms. *J. Comput. Chem.* **2001**, *22*, 976-984.
60. Rassolov, V. A.; Pople, J. A.; Ratner, M. A.; Windus, T. L. 6-31g* Basis Set for Atoms K through Zn. *J. Chem. Phys.* **1998**, *109*, 1223-1229.

61. Blaudeau, J.-P.; McGrath, M. P.; Curtiss, L. A.; Radom, L. Extension of Gaussian-2 (G2) Theory to Molecules Containing Third-Row Atoms K and Ca. *J. Chem. Phys.* **1997**, *107*, 5016-5021.
62. Francl, M. M.; Pietro, W. J.; Hehre, W. J.; Binkley, J. S.; Gordon, M. S.; DeFrees, D. J.; Pople, J. A. Self-Consistent Molecular Orbital Methods. XXIII. A Polarization-Type Basis Set for Second-Row Elements. *J. Chem. Phys.* **1982**, *77*, 3654-3665.
63. Gordon, M. S. The Isomers of Silacyclopropane. *Chem. Phys. Lett.* **1980**, *76*, 163-168.
64. Hariharan, P. C.; Pople, J. A. Accuracy of AH_n Equilibrium Geometries by Single Determinant Molecular Orbital Theory. *Mol. Phys.* **1974**, *27*, 209-214.
65. Hariharan, P. C.; Pople, J. A. The Influence of Polarization Functions on Molecular Orbital Hydrogenation Energies. *Theor. Chem. Acc.* **1973**, *28*, 213-222.
66. Hehre, W. J.; Ditchfield, R.; Pople, J. A. Self-Consistent Molecular Orbital Methods. XII. Further Extensions of Gaussian-Type Basis Sets for Use in Molecular Orbital Studies of Organic Molecules. *J. Chem. Phys.* **1972**, *56*, 2257-2261.
67. Ditchfield, R.; Hehre, W. J.; Pople, J. A. Self-Consistent Molecular-Orbital Methods. IX. An Extended Gaussian-Type Basis for Molecular-Orbital Studies of Organic Molecules. *J. Chem. Phys.* **1971**, *54*, 724-728.
68. Becke, A. D. Density-Functional Thermochemistry. III. The Role of Exact Exchange. *J. Chem. Phys.* **1993**, *98*, 5648-5652.
69. Lee, C.; Yang, W.; Parr, R. G. Development of the Colle-Salvetti Correlation-Energy Formula into a Functional of the Electron Density. *Phys. Rev. B.* **1988**, *37*, 785-789.
70. Vosko, S. H.; Wilk, L.; Nusair, M. Accurate Spin-Dependent Electron Liquid Correlation Energies for Local Spin Density Calculations: A Critical Analysis. *Can. J. Phys.* **1980**, *58*, 1200-1211.
71. Stephens, P. J.; Devlin, F. J.; Chabalowski, C. F.; Frisch, M. J. Ab Initio Calculation of Vibrational Absorption and Circular Dichroism Spectra Using Density Functional Force Fields. *J. Phys. Chem.* **1994**, *98*, 11623-11627.
72. Pople, J. A.; Headgordon, M.; Raghavachari, K. Quadratic Configuration-Interaction - a General Technique for Determining Electron Correlation Energies. *J. Chem. Phys.* **1987**, *87*, 5968-5975.
73. Greenwald, E. E.; North, S. W.; Georgievskii, Y.; Klippenstein, S. J. A Two Transition State Model for Radical-Molecule Reactions: A Case Study of the Addition of OH to C₂H₄. *J. Phys. Chem. A* **2005**, *109*, 6031-6044.
74. Cremer, D. Møller-Plesset Perturbation Theory: From Small Molecule Methods to Methods for Thousands of Atoms. *Wiley Interdiscip. Rev. Comput. Mol. Sci.* **2011**, *1*, 509-530.
75. Pople, J. A.; Head-Gordon, M.; Raghavachari, K. Corrections to Correlations Energies Beyond Fourth Order Moller-Plesset (MP4) Perturbation Theory. Contributions of Single, Double, and Triple Substitutions. *Int. J. Quantum Chem.* **1988**, *34*, 377-382.
76. Ochterski, J. W.; Petersson, G. A.; Jr., J. A. M. A Complete Basis Set Model Chemistry. V. Extensions to Six or More Heavy Atoms. *J. Chem. Phys.* **1996**, *104*, 2598-2619.
77. Baeza-Romero, M. T.; Blitz, M. A.; Goddard, A.; Seakins, P. W. Time-of-Flight Mass Spectrometry for Time-Resolved Measurements: Some Developments and Applications. *Int. J. Chem. Kinet.* **2012**, *44*, 532-545.
78. Taatjes, C. A. How Does the Molecular Velocity Distribution Affect Kinetics Measurements by Time-Resolved Mass Spectrometry? *Int. J. Chem. Kinet.* **2007**, *39*, 565-570.
79. Moore, S. B.; Carr, R. W. Molecular Velocity Distribution Effects in Kinetic Studies by Time-Resolved Mass-Spectrometry. *Int. J. Mass Spectrom. Ion Process.* **1977**, *24*, 161-171.
80. Atkinson, R.; Aschmann, S. M. Rate Constants for the Reaction of OH Radicals with a Series of Alkenes and Dialkenes at 295 K. *Int. J. Chem. Kinet.* **1984**, *16*, 1175-1186.
81. Atkinson, R.; Aschmann, S. M.; Winer, A. M.; Pitts, J. N. Rate Constants for the Reaction of OH Radicals with a Series of Alkanes and Alkenes at 299 +/- 2 K. *Int. J. Chem. Kinet.* **1982**, *14*, 507-516.

82. Campuzano-Jost, P.; Williams, M. B.; D'Ottone, L.; Hynes, A. J. Kinetics of the OH-Initiated Oxidation of Isoprene. *Geophys. Res. Lett.* **2000**, *27*, 693-696.
83. Campuzano-Jost, P.; Williams, M. B.; D'Ottone, L.; Hynes, A. J. Kinetics and Mechanism of the Reaction of the Hydroxyl Radical with *h*₈-Isoprene and *d*₈-Isoprene: Isoprene Absorption Cross Sections, Rate Coefficients, and the Mechanism of Hydroperoxyl Radical Production. *J. Phys. Chem. A* **2004**, *108*, 1537-1551.
84. Chuong, B.; Stevens, P. S. Measurements of the Kinetics of the OH-Initiated Oxidation of Isoprene. *J. Geophys. Res. Atmos.* **2002**, *107*, 4162.
85. Edney, E. O.; Kleindienst, T. E.; Corse, E. W. Room-Temperature Rate Constants for the Reaction of OH with Selected Chlorinated and Oxygenated Hydrocarbons. *Int. J. Chem. Kinet.* **1986**, *18*, 1355-1371.
86. Gill, K. J.; Hites, R. A. Rate Constants for the Gas-Phase Reactions of the Hydroxyl Radical with Isoprene, alpha- and beta-pinene, and Limonene as a Function of Temperature. *J. Phys. Chem. A* **2002**, *106*, 2538-2544.
87. Hites, R. A.; Turner, A. M. Rate Constants for the Gas-Phase Beta-Myrcene Plus OH and Isoprene Plus OH Reactions as a Function of Temperature. *Int. J. Chem. Kinet.* **2009**, *41*, 407-413.
88. Iida, Y.; Obi, K.; Imamura, T. Rate Constant for the Reaction of OH Radicals with Isoprene at 298 +/- 2 K. *Chem. Lett.* **2002**, 792-793.
89. Karl, M. et al. Kinetic Study of the OH-Isoprene and O₃-Isoprene Reaction in the Atmosphere Simulation Chamber, Saphir. *Geophys. Res. Lett.* **2004**, *31*, 4.
90. Kleindienst, T. E.; Harris, G. W.; Pitts, J. N. Rates and Temperature Dependences of the Reaction of OH with Isoprene, Its Oxidation-Products, and Selected Terpenes. *Environ. Sci. Tech.* **1982**, *16*, 844-846.
91. McQuaid, J. B.; Stocker, D. W.; Pilling, M. J. Kinetics of the Reactions of OH with 3-methyl-2-cyclohexen-1-one and 3,5,5-trimethyl-2-cyclohexen-1-one under Simulated Atmospheric Conditions. *Int. J. Chem. Kinet.* **2002**, *34*, 7-11.
92. Ohta, T. Rate Constants for the Reactions of Diolefins with OH Radicals in the Gas-Phase - Estimate of the Rate Constants from Those for Monoolefins. *J. Phys. Chem.* **1983**, *87*, 1209-1213.
93. Park, J.; Jongsma, C. G.; Zhang, R. Y.; North, S. W. OH/OD Initiated Oxidation of Isoprene in the Presence of O₂ and NO. *J. Phys. Chem. A* **2004**, *108*, 10688-10697.
94. Poppe, D.; Brauers, T.; Dorn, H. P.; Karl, M.; Mentel, T.; Schlosser, E.; Tillmann, R.; Wegener, R.; Wahner, A. OH-Initiated Degradation of Several Hydrocarbons in the Atmosphere Simulation Chamber Saphir. *J. Atmos. Chem.* **2007**, *57*, 203-214.
95. Vimal, D.; Pacheco, A. B.; Iyengar, S. S.; Stevens, P. S. Experimental and Ab Initio Dynamical Investigations of the Kinetics and Intramolecular Energy Transfer Mechanisms for the OH+1,3-butadiene Reaction between 263 and 423 K at Low Pressure. *J. Phys. Chem. A* **2008**, *112*, 7227-7237.
96. Zhang, D.; Zhang, R. Y.; Church, C.; North, S. W. Experimental Study of Hydroxyalkyl Peroxy Radicals from OH-Initiated Reactions of Isoprene. *Chem. Phys. Lett.* **2001**, *343*, 49-54.
97. Zhang, R. Y.; Suh, I.; Lei, W.; Clinkenbeard, A. D.; North, S. W. Kinetic Studies of OH-Initiated Reactions of Isoprene. *J. Geophys. Res. Atmos.* **2000**, *105*, 24627-24635.
98. Moré, J. J.; Sorensen, D. C. Computing a Trust Region Step. *SIAM J. Sci. Comput.* **1983**, *4*, 553-572.
99. Baulch, D. L. et al. Evaluated Kinetic Data for Combustion Modelling. *J. Phys. Chem. Ref. Data.* **1992**, *21*, 411-734.
100. Tully, F. P. Hydrogen-Atom Abstraction from Alkenes by OH, Ethene and 1-butene. *Chem. Phys. Lett.* **1988**, *143*, 510-514.
101. Atkinson, R.; Aschmann, S. M.; Tuazon, E. C.; Arey, J.; Zielinska, B. Formation of 3-Methylfuran from the Gas-Phase Reaction of OH Radicals with Isoprene and the Rate Constant for Its Reaction with the OH Radical. *Int. J. Chem. Kinet.* **1989**, *21*, 593-604.
102. Atkinson, R.; Tuazon, E. C.; Aschmann, S. M. Products of the Gas-Phase Reaction of the OH Radical with 3-methyl-1-butene in the Presence of NO. *Int. J. Chem. Kinet.* **1998**, *30*, 577-587.

103. Nordmeyer, T.; Wang, W.; Ragains, M. L.; Finlayson-Pitts, B. J.; Spicer, C. W.; Plastridge, R. A. Unique Products of the Reaction of Isoprene with Atomic Chlorine: Potential Markers of Chlorine Atom Chemistry. *Geophys. Res. Lett.* **1997**, *24*, 1615-1618.
104. Ragains, M. L.; Finlayson-Pitts, B. J. Kinetics and Mechanism of the Reaction of Cl Atoms with 2-Methyl-1,3-butadiene (Isoprene) at 298 K. *J. Phys. Chem. A*. **1997**, *101*, 1509-1517.
105. Jenkin, M. E.; Young, J. C.; Rickard, A. R. The MCM V3.3.1 Degradation Scheme for Isoprene. *Atmos. Chem. Phys.* **2015**, *15*, 11433-11459.
106. Peeters, J.; Boullart, W.; Pultau, V.; Vandenberg, S.; Vereecken, L. Structure-Activity Relationship for the Addition of OH to (Poly)Alkenes: Site-Specific and Total Rate Constants. *J. Phys. Chem. A* **2007**, *111*, 1618-1631.
107. MathWorks, I., *Matlab and Optimization Toolbox Release R2016a*. Natwick : Math Works Inc.: 2016.
108. Dibble, T. S. Isomerization of OH-Isoprene Adducts and Hydroxyalkoxy Isoprene Radicals. *J. Phys. Chem. A* **2002**, *106*, 6643-6650.
109. Papadimitriou, V. C.; Karafas, E. S.; Gierczak, T.; Burkholder, J. B. CH₃CO + O₂ + M (M = He, N₂) Reaction Rate Coefficient Measurements and Implications for the OH Radical Product Yield. *J. Phys. Chem. A* **2015**, *119*, 7481-7497.
110. Baeza-Romero, M. T.; Glowacki, D. R.; Blitz, M. A.; Heard, D. E.; Pilling, M. J.; Rickard, A. R.; Seakins, P. W. A Combined Experimental and Theoretical Study of the Reaction between Methylglyoxal and OH/OD Radical: OH Regeneration. *Phys. Chem. Chem. Phys.* **2007**, *9*, 4114-4128.
111. Martins, G. et al. Valence Shell Electronic Spectroscopy of Isoprene Studied by Theoretical Calculations and by Electron Scattering, Photoelectron, and Absolute Photoabsorption Measurements. *Phys. Chem. Chem. Phys.* **2009**, *11*, 11219-11231.
112. Troe, J.; Ushakov Vladimir, G. Representation of "Broad" Falloff Curves for Dissociation and Recombination Reactions. *Z. Phys. Chem.* **2014**, *228*, 1-10.

